Panchromatic Properties of 99,000 Galaxies Detected by SDSS, and (some by) ROSAT, GALEX, 2MASS, IRAS, GB6, FIRST, NVSS and WENSS Surveys

M. Obrić[1,2], Ž. Ivezić[2], P.N. Best[3], R.H. Lupton[4], C. Tremonti[6], J. Brinchmann[5],
M.A. Agüeros[2], G.R. Knapp[4], J.E. Gunn[4], C.M. Rockosi[7], D. Schlegel[4], D. Finkbeiner[4],
M. Gaćeša[13,10], V. Smolčić[12,10], S.F. Anderson[2], W. Voges[8], M. Jurić[4],
R.J. Siverd[4], W. Steinhardt[4], A.S. Jagoda[4], M.R. Blanton[9], D.P. Schneider[11]

[1] *Kapteyn Astronomical Institute, University of Groningen, P.O. Box 800, Groningen 9700 AV, The Netherlands*
[2] *University of Washington, Department of Astronomy, Box 351580, Seattle, WA 98195-1580, USA*
[3] *Institute for Astronomy, Royal Observatory Edinburgh, Blackford Hill, Edinburgh EH9 3HJ, UK*
[4] *Princeton University Observatory, Peton Hall, Princeton, NJ 08544-1001, USA*
[5] *Max-Planck-Institute für Astrophysik, D-85748, Garching, Germany*
[6] *Hubble Fellow, University of Arizona, Steward Observatory, 933 N. Cherry Ave., Tucson, AZ 85721, USA*
[7] *University of California–Santa Cruz, 1156 High St., Santa Cruz, CA 95060, USA*
[8] *Max-Planck-Institute für Extraterrestrische Physik, Karl-Schwarzschild-Str. 1, Postfach 1317, D-85741 Garching, Germany*
[9] *The New York University, Physics Department, 4 Washington Place, New York, NY 10003, USA*
[10] *University of Zagreb, Physics Department, Bijenička cesta 32, 10000 Zagreb, Croatia*
[11] *Department of Astronomy and Astrophysics, 525 Davey Laboratory, University Park, PA 16802, USA*
[12] *Max-Planck-Institut für Astronomie, Königstuhl 17, Heidelberg, D-69117, Germany*
[13] *University of Connecticut, Physics Department, 2152 Hillside Road, Storrs, CT 06269-3046, USA*

5 February 2008

ABSTRACT

We discuss the panchromatic properties of 99,088 galaxies selected from the Sloan Digital Sky Survey Data Release 1 "main" spectroscopic sample (a flux-limited sample for 1360 deg^2). These galaxies are positionally matched to sources detected by ROSAT, GALEX, 2MASS, IRAS, GB6, FIRST, NVSS and WENSS. The matching fraction varies from $< 1\%$ for ROSAT and GB6 to $\sim 40\%$ for GALEX and 2MASS. In addition to its size, the advantages of this sample are well controlled selection effects, faint flux limits and the wealth of measured parameters, including accurate X-ray to radio photometry, angular sizes, and optical spectra. We find strong correlations between the detection fraction at other wavelengths and optical properties such as flux, colors, and emission-line strengths. For example, $\sim 2/3$ of SDSS "main" galaxies classified as AGN using emission-line strengths are detected by 2MASS, while the corresponding fraction for star-forming galaxies is only $\sim 1/10$. Similarly, over 90% of galaxies detected by IRAS display strong emission lines in their optical spectra, compared to $\sim 50\%$ for the whole SDSS sample. Using GALEX, SDSS, and 2MASS data, we construct the UV-IR broad-band spectral energy distributions for various types of galaxies, and find that they form a nearly one-parameter family. For example, the SDSS u- and r- band data, supplemented with redshift, can be used to "predict" K-band magnitudes measured by 2MASS with an rms scatter of only 0.2 mag. When a dust content estimate determined from SDSS spectra with the aid of models is also utilized, this scatter decreases to 0.1 mag and can be fully accounted for by measurement uncertainties. We demonstrate that this interstellar dust content, inferred from optical SDSS spectra by Kauffmann et al. (2003a), is indeed higher for galaxies detected by IRAS and that it can be used to "predict" measured IRAS 60 μm flux density within a factor of two using only SDSS data. We also show that the position of a galaxy in the emission-line-based Baldwin-Phillips-Terlevich diagram is correlated with the optical light concentration index and $u-r$ color determined from the SDSS broad-band imaging data, and discuss changes in the morphology of this diagram induced by requiring detections at other wavelengths. Notably, we find that SDSS "main" galaxies detected by GALEX include a non-negligible fraction (10-30%) of AGNs, and hence do not represent a clean sample of starburst galaxies. We study the IR-radio correlation and find evidence that its slope may be different for AGN and star-forming galaxies and related to the H_α/H_β line strength ratio.

Key words: surveys – galaxies: fundamental parameters – galaxies: active – galaxies: starburst – infrared: galaxies – radio continuum: galaxies – ultraviolet: galaxies – X-rays: galaxies.

1   INTRODUCTION

The study of global galaxy properties has been recently invigorated by modern sensitive large-area surveys across a wide wavelength range. The Sloan Digital Sky Survey (SDSS, York et al. 2000, for more details see Appendix A1) stands out because it has already provided near-UV to near-IR five-color imaging data and high-quality spectra (R∼1800) for over 500,000 galaxies. The "main" spectroscopic galaxy sample is defined by a simple r-band flux limit (Strauss et al. 2002), and will include close to 1,000,000 galaxies.

A number of detailed galaxy studies based on SDSS data have already been published. Strateva et al. (2001) and Shimasaku et al. (2001) demonstrated a tight correlation between the $u - r$ color, concentration of the galaxy's light profile, and morphology. Blanton et al. (2003) presented the SDSS galaxy luminosity function, and Kauffmann et al. (2003ab) determined and analyzed stellar masses and star-formation histories for 100,000 SDSS galaxies.

In addition to "stand-alone" studies based on only SDSS data, SDSS can be used as a cornerstone for panchromatic studies of galaxies aided by recent surveys at wavelengths outside the optical range (0.3-1 μm). The special role of SDSS in such studies is due to its rich optical information, in particular high-quality spectra and photometry. Nevertheless, galaxies emit a substantial fraction of their bolometric flux outside the wavelength range accessible to SDSS. For example, in starburst and Seyfert 2 galaxies the mid/far-IR wavelength range is the most important contributor to the bolometric flux, e.g. Schmitt et al. (1997). Information obtained by other surveys offers important observational constraints for models of galaxy formation and evolution.

Numerous studies that utilize SDSS and surveys at other wavelengths have already been published. For example, Finlator et al. (2000) analyzed the properties of point sources detected by SDSS and Two Micron All Sky Survey (2MASS), and Ivezić et al. (2001a) discussed the colors and counts of SDSS sources detected by SDSS, 2MASS, and FIRST surveys. Ivezić et al. (2002) cross-correlated SDSS and the survey Faint Images of the Radio Sky at Twenty Centimeters (FIRST), and analyzed the optical and radio properties of quasars and galaxies. Bell et al. (2003) used SDSS and 2MASS data to estimate the baryonic mass functions of galaxies, and Anderson et al. (2003) studied the properties of AGN galaxies detected by SDSS and ROSAT. Best et al. (2005ab) studied radio galaxies, Chang et al. (2005) analyzed the SDSS-2MASS colors of elliptical galaxies, and Goto (2005) and Pasquali, Kauffmann & Heckman (2005) studied the optical properties of SDSS galaxies detected by IRAS. A detailed analysis of rest-frame colors in the Strömgren system synthesized from SDSS spectra was presented by Smolčić et al. (2006). They found that the galaxy distribution in the resulting color-color diagrams forms a very narrow locus with a width of only 0.03 mag. This finding agrees well with the conclusion by Yip et al. (2004), based on a principal component analysis of SDSS spectra, that galaxy spectra can be described by a small number of eigenspectra.

Here we cross-correlate the catalog of galaxies from SDSS Data Release 1 (Abazajian et al. 2003) with cata-

logs of sources detected by ROSAT (X ray), GALEX (UV), 2MASS (near-IR), IRAS (mid/far-IR), GB6 (6 cm), FIRST (20 cm), NVSS (20 cm), and WENSS (92 cm). References and a description of each survey are listed in Appendix A. The panchromatic galaxy samples discussed here are ∼10-100 times larger than those used in older pre-SDSS studies. In addition, they are selected by simple flux limits, and benefit from a wealth of accurately measured parameters including X-ray to radio photometry, angular sizes, and optical spectra. The main aim of this paper is to quantify the fraction and basic properties of SDSS "main" galaxies detected by other surveys using a uniform approach for all analyzed surveys. However, due to the size and quality of the resulting samples, even a simple, preliminary analysis presented here is sufficient to yield a wealth of additional results.

We describe our matching and analysis methods in Section 2. In Section 3 we discuss the detection fraction of SDSS galaxies by other surveys, and in Section 4 we present a preliminary analysis of some panchromatic properties of galaxies in our sample. We discuss and summarize our results in Section 5.

2   MATCHING AND ANALYSIS METHODS

There are 99,825 unique galaxies in the Sloan Digital Sky Survey Data Release 1 "main" spectroscopic sample[1], a sample limited by Petrosian magnitude, $r_{Pet} < 17.77$ and covering 1360 deg^2 (for more detailed description see Stoughton et al. 2002 and Strauss et al. 2002). We further restrict the sample by requiring the redshifts to lie in the range $0.01 \leqslant z \leqslant 0.30$ and obtain the sample of 99,088 galaxies analyzed here. For each galaxy, SDSS provides numerous properties measured from 5-color imaging data, such as astrometry, photometry, and morphological information, as well as high-quality spectra. In addition to standard spectroscopic parameters automatically measured by the spectroscopic pipeline, we also utilize emission line measurements described by Kauffmann et al. (2003a). We emphasize that the SDSS astrometry is very accurate (∼0.1 arcsec, Pier et al. 2002), which significantly simplifies the matching algorithm.

For each SDSS galaxy, we search for the two nearest neighbors in each of the eight catalogs. We accept the nearest neighbor as a true association if its distance is smaller than the catalog-dependent matching radius listed in Table 1. The matching radius for each catalog was determined by analyzing the distribution of distances between the quoted position in the catalog and the SDSS position, and corresponds to a ∼ 3σ cutoff[2]. Due to either high astrometric accuracy of other catalogs (e.g., 2MASS), or their low source surface density (e.g., IRAS), the matching contamination rate (fraction of false associations) is typically very low (< 1%) at non-radio wavelengths and ∼ 10% for the four radio surveys, as implied by both the source density

---

[1] The recent SDSS Data Release 4 contains spectra for 565,715 galaxies, see www.sdss.org
[2] The distance distribution for the SDSS-NVSS sample is better fit by a sum of two Gaussians. However, this behavior has no significant consequence for the matching completeness and contamination.

Table 1. Catalogs, their wavelength range, matching radius, total number of matches (for SDSS total number of galaxies), false match probability for the adopted matching radius, and, in the bottom table, matching fractions for all galaxies and for each galaxy class. False match probabilities are computed from the source density in the matched catalogs, and are consistent with the random matching rate when SDSS positions are offset by 1 deg in declination. The matching fractions in the bottom table are corrected for the difference in area covered by each catalog and the area covered by SDSS DR1. Emission/No emission tags in the bottom table refer to whether or not the emission lines were detected in a galaxy (see text). The bottom row lists the surface density of each galaxy subsample in the SDSS DR1 catalog.

Catalog	Wavelength	Matching distance ["]	All [absolute #]	False match probability [%]	False associations [%]
SDSS	NUV-NIR	-	99088	-	-
ROSAT RASS	X-ray	30	267	0.056	8.9
GALEX	UV	6	866	0.796	1.9
2MASS XSC	near-IR	1.5	19184	0.002	< 1
IRAS FSC	far-IR	30	1736	0.013	< 1
GB6	6 cm	20	132	0.003	14
FIRST	20 cm	3	3402	0.037	1.0
NVSS	20 cm	15	3478	0.291	8.3
WENSS	92 cm	20	363	0.227	9.1

Catalog	All [%]	No emission [%]	Emission [%]	AGN [%]	SF [%]	Unknown [%]
ROSAT RASS	0.63	0.63	0.46	0.87	0.24	0.23
GALEX	42.0	24.1	67.7	27.9	82.1	93.3
2MASS XSC	38.1	35.7	39.6	63.8	10.7	34.0
IRAS FSC	1.77	0.14	2.95	3.01	1.73	3.54
GB6	0.22	0.15	0.09	0.21	0.02	0.02
FIRST	3.86	2.76	4.68	8.06	0.98	3.40
NVSS	3.51	2.85	3.52	5.02	1.66	3.25
WENSS	2.50	3.23	1.40	2.46	0.49	1.01
SDSS [#/deg^2]	72.86	39.38	33.48	11.81	7.54	13.44

in the matched catalogs, and the matching rate when SDSS positions are offset by 1 deg in declination. The fraction of cases where two sources in other catalogs are found within the matching radius is typically small ($< 1\%$); in these cases we simply take the nearest neighbor to represent the true association. This fraction is sufficiently low that none of the conclusions presented in this paper change when both neighbors are excluded.

Before we proceed with the discussion of matching rate for each catalog, we describe our analysis methods in the next two sections.

2.1 The global optical properties of galaxies in the SDSS DR1 main spectroscopic sample

The first step in analyzing galaxies detected at other wavelengths is to compare their distribution in the optical parameter space to that for the whole SDSS sample. The parameters measured by the SDSS photometric pipeline *photo* (Lupton et al. 2002) are numerous ($\sim$100), and we limit our preliminary analysis to the distribution of galaxies in optical color-magnitude-redshift space.

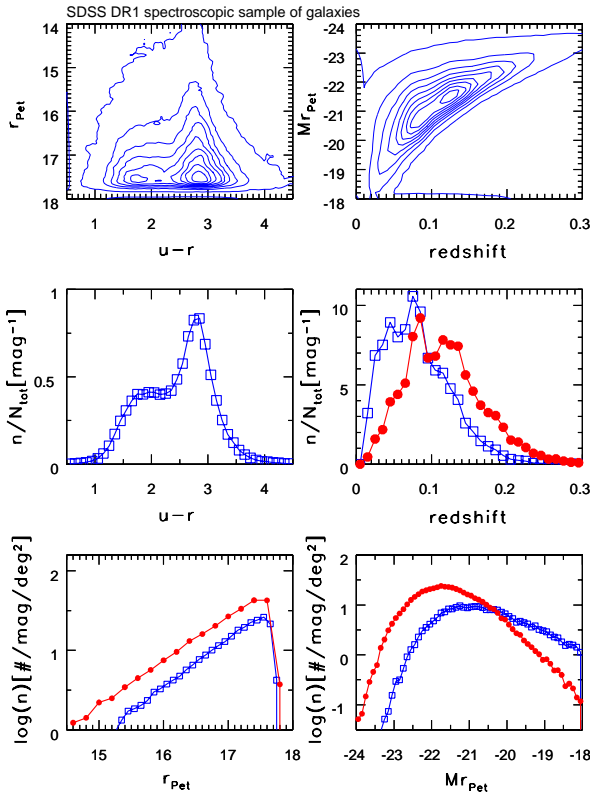#### 2.1.1 Color-magnitude-redshift distributions

SDSS galaxies are not randomly distributed in the space spanned by apparent (or absolute) magnitude, color, and redshift. As shown by Strateva et al. (2001), and discernible in Fig. 1, galaxies show a bimodal $u - r$ color distribution (hereafter, optical SDSS colors are constructed using

so-called "model" magnitudes; for details see Stoughton et al. 2002). Galaxies with $u - r < 2.22$ tend to be spiral galaxies, and those with $u - r > 2.22$ elliptical galaxies (see also Shimasaku et al. 2001 and Baldry et al. 2003). Because the spiral/blue galaxies tend to have lower luminosities than elliptical/red galaxies (bottom right panel), the former are typically found at lower redshifts in the flux-limited SDSS sample than are the latter. Blanton et al. (2003) give a detailed analysis of the dependence of luminosity function on galaxy type. Note that the "features" in the middle right panel of Figure 1 are due to the large scale structure of galaxies. The differential number counts of both color types are well described by $\log(n) = C + 0.6\, r_{Pet}$ (see also Yasuda et al. 2001). We will use diagrams such as that shown in Fig. 1 to compare the distributions of galaxies detected at other wavelengths to the distribution of all SDSS galaxies.

2.1.2 The distribution of emission-line galaxies in the Baldwin-Phillips-Terlevich diagram

In addition to the overall comparison of galaxy distributions in diagrams shown in Fig. 1, we analyze the behavior of three subsamples defined by their emission line properties: galaxies without emission lines, and emission-line galaxies separated into star-forming and AGNs. To classify a galaxy as an emission-line galaxy, we follow Kauffmann et al. (2003a) and require a 3σ significant detection of the H_α, H_β, $[NII\,6583]$ and $[OIII\,5007]$ lines. To classify emission-line galaxies as star-forming or AGN, we use the standard BPT diagram (Baldwin, Phillips & Terlevich, 1981).
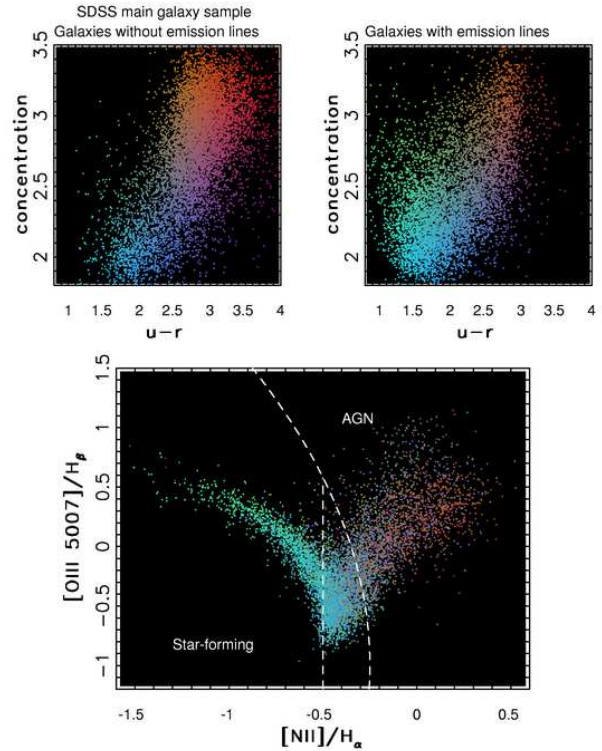
The top two panels in Fig. 2 compare the distribution

Figure 1. Color-magnitude-redshift distributions for SDSS DR1 "main" galaxies ($r_{Pet} < 17.77$). The top two panels show the distribution of galaxies using linearly spaced contours, in steps of 10%. The middle left panel shows the $u - r$ distribution of galaxies. Galaxies with $u - r < 2.22$ tend to be spiral/blue galaxies, and those with $u - r > 2.22$ elliptical/red galaxies (Strateva et al. 2001). Using this separation, the middle right panel shows the redshift (probability) distributions for blue (open squares) and red (dots) subsets. The same symbols are used to display their differential apparent magnitude (bottom left) and absolute magnitude (bottom right) distributions.

of galaxies without and with emission lines in the concentration index vs. $u-r$ diagram. Galaxies without emission lines tend to have larger concentration index and redder $u-r$ than galaxies with emission lines. The dots in these two panels are two-dimensionally color coded according to their concentration index and $u - r$ color. The same color-coding scheme is used in the bottom panel, which shows the BPT diagram for emission-line galaxies. *There is a strong correspondence between the position of a galaxy in the BPT diagram and its position in the concentration index vs. $u-r$ diagram.* Galaxies in the "star-forming branch" with small $[NII]/H_\alpha$ ratio, for a given $[OIII\,5007]/H_\beta$ ratio, have predominantly blue $u-r$ colors and small concentration index, while AGNs have redder $u - r$ colors and large concentration index. Furthermore, the distribution of *emission-line* galaxies in the BPT diagram is also correlated with $u - r$ and concentration index.

In the subsequent analysis, we separate emission-line galaxies into three groups according to their position in the BPT diagram: AGNs, star-forming, and "unknown". The

Figure 2. The top two panels compare the distribution of galaxies without (left) and with (right) emission lines in the concentration index vs. $u - r$ diagram. The dots are two-dimensionally color coded according to their concentration index and $u - r$ color. The same color-coding scheme is used in the bottom panel, which shows the BPT diagram for emission-line galaxies (note that the line flux ratios are expressed on a logarithmic scale). Emission-line galaxies can be separated into three groups according to their position in the BPT diagram: AGNs, star-forming, and "unknown", using the separation boundaries outlined by the dashed lines. Note the strong correlation between position in the BPT diagram and $u - r$.

adopted separation boundaries are shown by the dashed lines, and are designed to produce robust clean samples of AGN and star-forming galaxies (for alternative approaches see Hao et al. 2005, and references therein; for the aperture effects due to 3 arcsec fiber diameter see, e.g., Kauffmann et al. 2003a and Kewley et al. 2005). The "unknown" category is found at the join of the two branches, and it is not obvious from the displayed data to which class these galaxies belong. While their concentration index and $u-r$ color indicate that they may be star-forming galaxies, their IR colors and redshift distribution (see Section 4) suggest that they are more similar to AGN galaxies. Of course, it is possible that these objects are star-forming galaxies that host an AGN.

The comparison of the distributions of AGN and star-forming galaxies in magnitude-color-redshift space is shown in Fig. 3. As discussed above, the two types of galaxies, classified using emission lines, have remarkably different $u - r$ distributions (see middle left panel). Furthermore, star-forming galaxies tend to have smaller luminosities than
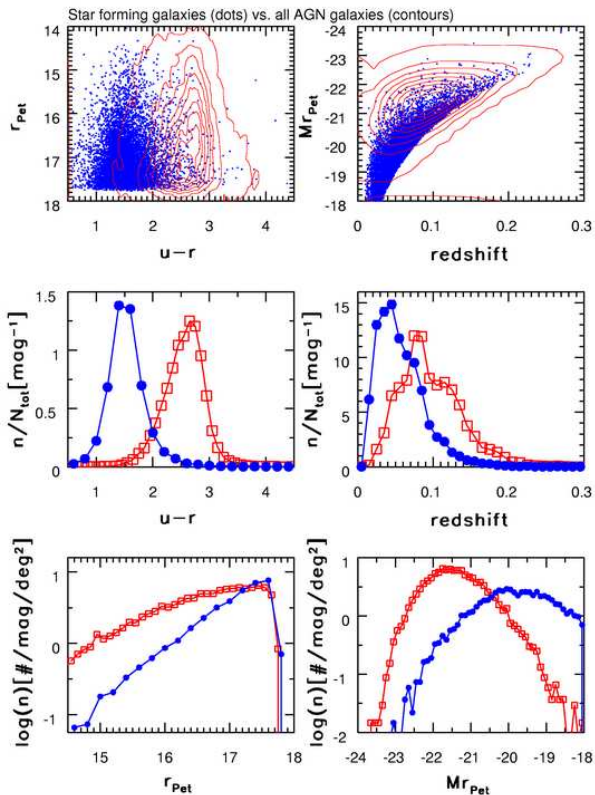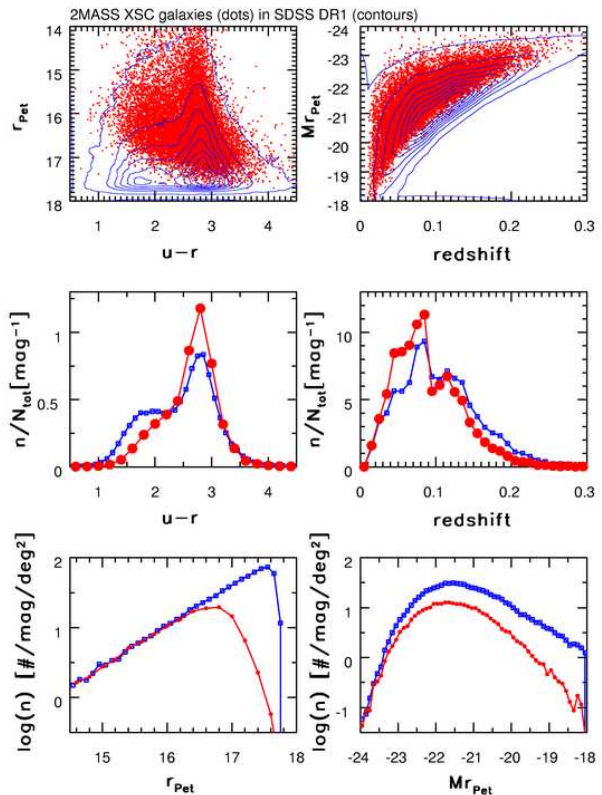
Figure 3. The comparison of distributions of AGN (contours, squares) and star-forming (dots, filled circles) emission-line galaxies in magnitude-color-redshift space. Note remarkable differences in their broad-band imaging properties (especially $u - r$) showing the correlation of spectroscopic and photometric properties.

AGNs, and hence are observed at lower redshifts in the flux-limited SDSS sample. They also have very different differential number counts - the counts of AGN galaxies are flatter $(d(\log N)/dr \sim 0.3)$ than those of star-forming galaxies (and those of the whole SDSS sample). For detailed studies of the optical properties of star-forming and AGN galaxies, see e.g. Brinchmann et al. (2004), Tremonti et al. (2004), Heckman et al. (2004), and references therein.

3 WHAT TYPES OF SDSS GALAXIES ARE DETECTED AT OTHER WAVELENGTHS?

The detection fraction of SDSS galaxies at other wavelengths is a strong function of optical properties such as flux, $u - r$, and emission-line strengths. In this analysis, we have taken into account the most important selection effects, namely: observational biases caused by varying survey depths, astrophysical effects such as intrinsically different color distributions for different galaxy types, and K correction (Gunn & Oke 1975) coupled with bias in redshift. The size and quality of our sample, in addition to its well controlled selection criteria, allow us to separate observational and astrophysical effects, and to study intrinsic correlations amongst numerous measured galaxy properties.

The matching fraction varies from $< 1\%$ for ROSAT

Figure 4. The comparison of color-magnitude-redshift distributions for all SDSS DR1 "main" galaxies (contours, and histograms marked with small squares) and those listed in 2MASS XSC (dots, and histograms marked with large dots). 2MASS XSC galaxies are biased towards red galaxies, larger luminosities, and smaller redshifts. The 2MASS XSC catalog is essentially complete for galaxies with $r_{Pet} < 16.3$ (see bottom left panel).

and GB6 to $\sim 40\%$ for GALEX and 2MASS (Table 1). We start the discussion with the 2MASS, continue toward longer wavelengths, and then proceed from optical toward shorter wavelengths.

3.1 2MASS survey

The distribution of SDSS galaxies detected by 2MASS[3] in the color-magnitude-redshift space is compared to the distribution of all SDSS galaxies in Fig. 4. The requirement that a galaxy is detected and resolved by 2MASS (i.e., the XSC sample, see Appendix A4) introduces a bias towards red galaxies and lower redshift as shown in the middle two panels. The SDSS-2MASS XSC catalog is essentially complete[4] for galaxies brighter than $r_{Pet} \sim 16.3$ (bottom left panel, see also McIntosh et al. 2005).

The color-dependent incompleteness of the 2MASS XSC catalog for galaxies with $r_{Pet} \gtrsim 16.3$ is due to the

---

[3] We analyze only resolved 2MASS sources listed in the 2MASS XSC catalog; see Appendix A4 for more details.
[4] Here "essentially complete" implies a completeness of $\sim 99\%$, as demonstrated by the direct comparison of the full SDSS and 2MASS overlap (see Finlator et al. 2000 and Ivezić et al. 2001b).
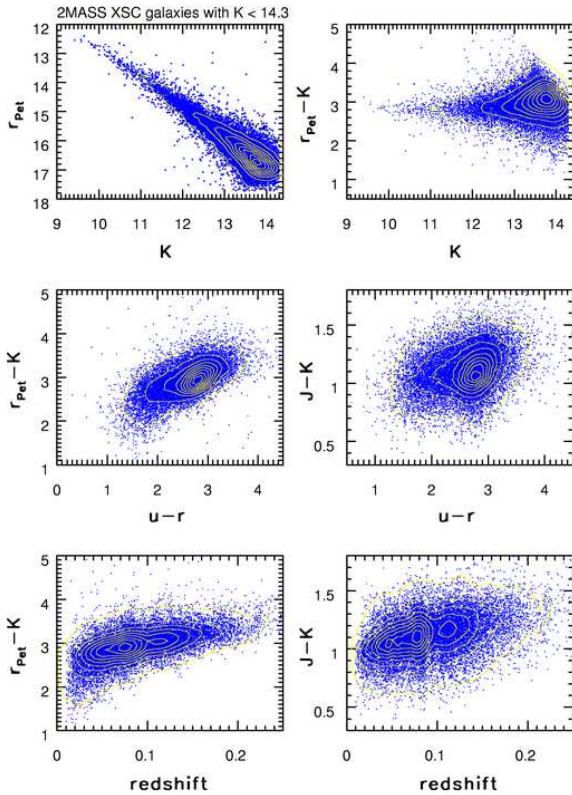
Figure 5. The optical and IR colors of SDSS galaxies listed in 2MASS XSC.

2MASS faint limit, coupled with the optical/IR color distribution of galaxies. We adopted $K = 14.3$, which corresponds to a $\sim 10\sigma$ detection; the K-band differential counts of 2MASS XSC galaxies indicate that the catalog is complete to about K=13.5. Fig. 5 shows the optical/IR magnitude and color distributions of SDSS-2MASS galaxies. We use 2MASS "default" magnitudes (see Jarret et al. 2000) and do not correct for the differences between AB (SDSS) and Vega (2MASS) magnitudes[5]. These differences are $m_0 = m_{AB} - m_{Vega}$, where $m_0(J) = 0.89$, $m_0(H) = 1.37$, and $m_0(K) = 1.84$ (see Finlator et al. 2000). Most galaxies have $r_{Pet} - K$ in the range 2–3.5. Thus, the bluest galaxies are brighter than the 2MASS faint limit only if they have $r_{Pet} < 16.3$. For $r_{Pet} > 16.3$ only galaxies with $r_{Pet} - K$ redder than $r_{Pet} - 14.3$ are sufficiently bright in the K-band, and at $r_{Pet} = 17.8$ practically no galaxies are listed in 2MASS XSC. This bias explains why the fraction of red galaxies in SDSS-2MASS sample is higher than among all SDSS galaxies (80% vs. 66%, with the blue/red separation defined by $u - r$=2.22). Since red galaxies tend to be more luminous than blue galaxies (e.g., Blanton et al. 2003), this color bias also explains why 2MASS-SDSS galaxies are biased towards larger luminosities.

---

[5] For completeness, the AB-to-Vega offsets for SDSS bands are $m_0(u) = 0.94$, $m_0(g) = -0.08$, $m_0(r) = 0.17$, $m_0(i) = 0.40$, and $m_0(z) = 0.57$ (see http://www.sdss.org/ for details on the transformations)

As the bottom two panels in Fig. 5 demonstrate $r_{Pet} - K$ and $J - K$ depend on redshift. This correlation (K correction), coupled to the color effects discussed above, introduces a dependence of the detection fraction on redshift. It is also an important effect to consider when comparing the colors of various subsamples that may have different redshift distributions, as we further discuss in Section 4.2.

3.1.1 Predicting 2MASS K-band flux from UV/optical SDSS fluxes

The optical-IR color, $r_{Pet} - K$, is correlated with the UV-optical $u-r$ color, as shown in the middle left panel in Fig. 5. This correlation indicates that it is possible to estimate the K-band flux using only SDSS data, and is consistent with the fact that galaxies form a nearly one-dimensional sequence in various optical color-color diagrams constructed with SDSS data. The correlation among colors is especially tight for optical rest-frame colors, with a scatter of only $\sim$0.03 mag perpendicular to the locus (Smolčić et al. 2006). The $r_{Pet} - K$ vs. $u-r$ correlation demonstrates that this one-dimensionality of broad-band galaxy spectral energy distributions (SEDs) extends to near-IR wavelengths.

In order to quantitatively assess to what extent near-IR flux is correlated with optical fluxes, we determine the K-band flux from $K_{SDSS} = r_{Pet} - (r - K)^*$, where r_{Pet} is the SDSS r-band Petrosian magnitude and $(r - K)^*$ is a best fit to the observed $r_{Pet} - K$ colors for SDSS/2MASS galaxies sampled from SDSS. We use UV/visual fluxes (u- and r-bands) to fit the $r_{Pet} - K$ color because this is the "hardest" wavelength combination with most astrophysical implications. According to "common wisdom", such a relationship should not be very accurate due to the effects of starbursts and dust extinction. Predicting, for example, 2MASS J-band flux from SDSS z-band flux is trivial because these two bands are adjacent in wavelength space. We also take into account the K correction (see the bottom left panel in Fig. 5), and fit the following functional form

$$(r-K)^* = A+B\,(u-r)+C\,(u-r)^2+D\,(u-r)^3+E\,z_r+F\,z_r^2 \quad (1)$$

where z_r is redshift.

The motivation for this functional form is the behavior of the $r - K$ color shown in the top panel in Fig. 6. The $r - K$ color also seems to be a well-defined function of the position in the $g - r$ vs. $u - g$ color-color diagram, shown in the bottom panel in Fig. 6, but the scatter around the median values in each bin is larger than for the $u - r$ vs. redshift diagram (this is essentially due to larger uncertainty of photometric redshifts that are implied by the position of a galaxy in the $g - r$ vs. $u - g$ diagram, in comparison to spectroscopic redshifts).

With the best-fit values (A, B, C, D, E, F)= (1.115, 0.940, -0.165, 0.00851, 4.92, -9.10), this relation predicts 2MASS K-band magnitudes with an rms scatter of only 0.20 mag. The residuals between the fitted and measured values depend on neither color nor redshift, and are nearly Gaussian (see the two middle panels in Fig. 7). However, there is a correlation between the residuals and the optical galaxy size, parametrized by R_{50}^z, the radius enclosing 50% of the Petrosian flux in the z-band (for details see Stoughton et al. 2002, and Strauss et al. 2002). To correct for these aperture and resolution effects, which presumably depend
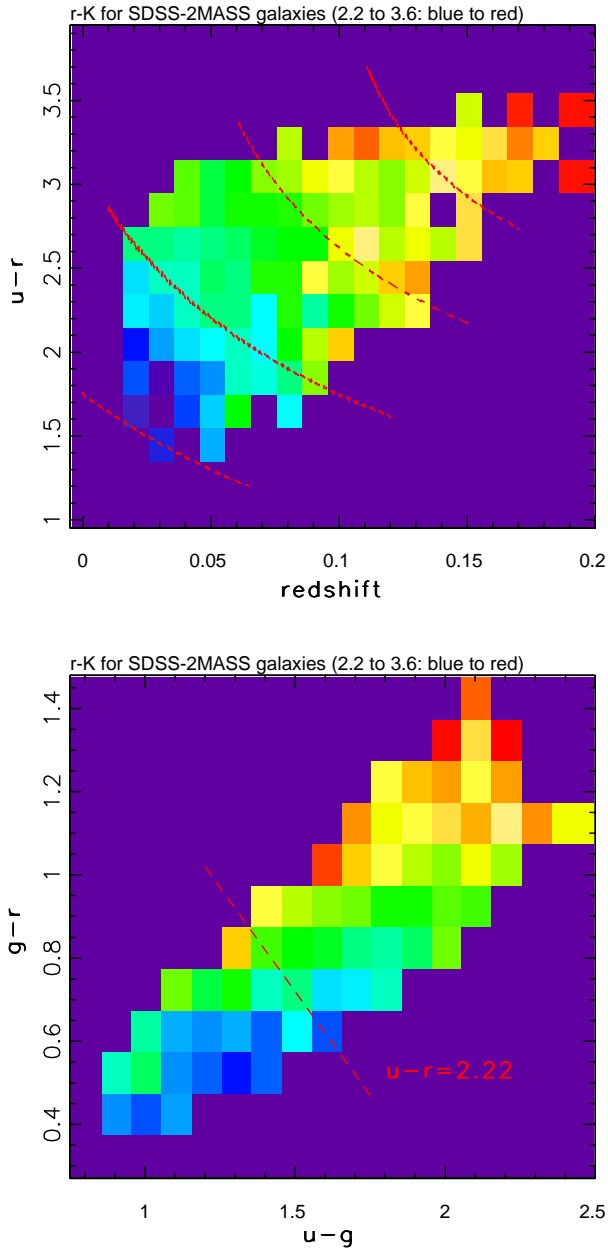
Figure 6. The top panel shows the median $r - K$ color in small $u - r$ vs. redshift bins. The median color is color-coded blue to red in the 2.2–3.6 range with a linear stretch. Bins with fewer than 3 galaxies are shown with magenta color. The distribution of the root-mean-scatter of $r - K$ color per bin has a median of 0.2 mag and a width of 0.08 mag. The dashed lines represent contours of constant $r - K$ (2.3, 2.7, 3.0 and 3.2) given by eq.1. The bottom panel shows the median $r - K$ color in small $g - r$ vs. $u - g$ color bins, with analogous color coding. The distribution of the root-mean-scatter of $r - K$ color per bin has a median of 0.23 mag and a width of 0.10 mag. The dashed line shows the boundary between blue and red galaxies ($u - r$=2.22) proposed by Strateva et al. (2001).
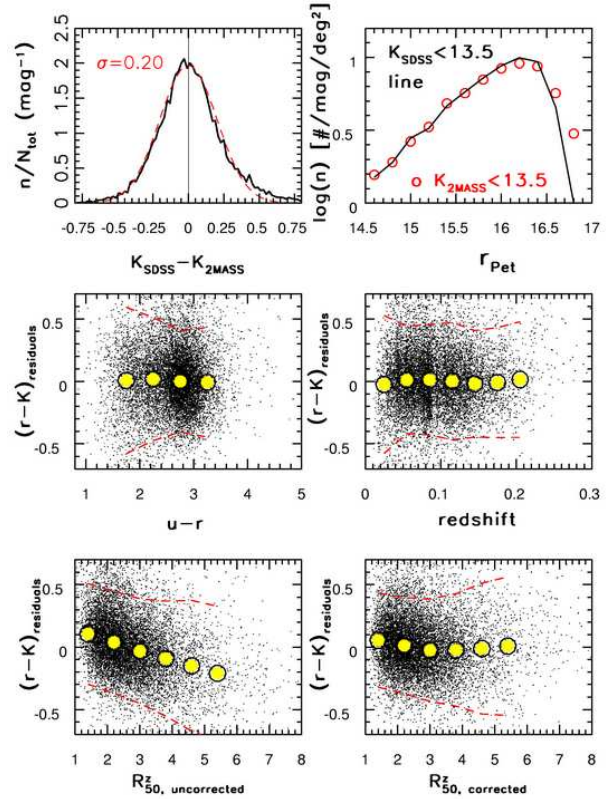
Figure 7. The solid line in the top left panel shows the distribution of differences between SDSS-predicted and 2MASS-measured K-band flux, using eq. 1. The dashed line is a Gaussian with $\sigma = 0.20$ mag. The right panel shows the r-band counts of SDSS-predicted (line) and 2MASS-measured (symbols) galaxies with $K < 13.5$. The two middle panels show the dependence of residuals between predicted and measured K-band magnitudes on the $u - r$ color (left) and redshift (right). The bottom left panel show the dependence of the same residuals on R_{50}^z, the radius enclosing 50% of the Petrosian flux in the z-band, before (left) and after (right) correcting for this effect. In the lower four panels, large yellow circles represent medians and 2σ envelope is given by red dashed curves.

on galaxy profile[6], or nearly equivalently on galaxy color (Strateva et al. 2001), we add to the right hand side of the eq. 1 $\Delta(r - K)^* = (0.496 - 0.154\,R_{50}^z)$ for galaxies with $u - r < 2.22$ and $\Delta(r - K)^* = (0.107 - 0.045\,R_{50}^z)$ for redder galaxies. This correction has a negligible effect on the rms scatter in the predicted K magnitude, and only removes a correlation of $K_{SDSS} - K_{2MASS}$ residuals with galaxy size (see the two bottom panels in Fig. 7).

The distribution of differences between the predicted and measured K-band magnitudes is shown in Fig. 7 (top left panel). The median residuals, as a function of $u - r$ and z_r, do not exceed 0.03 mag, and the rms scatter decreases to 0.15 mag at the bright end ($K < 12$). The top right panel in Fig. 7 compares the differential number counts as a function of r_{Pet} for galaxies with $K < 13.5$, where the latter condition is imposed using measured and predicted values.

---

[6] This assumption was recently verified by Chang et al. (2005).
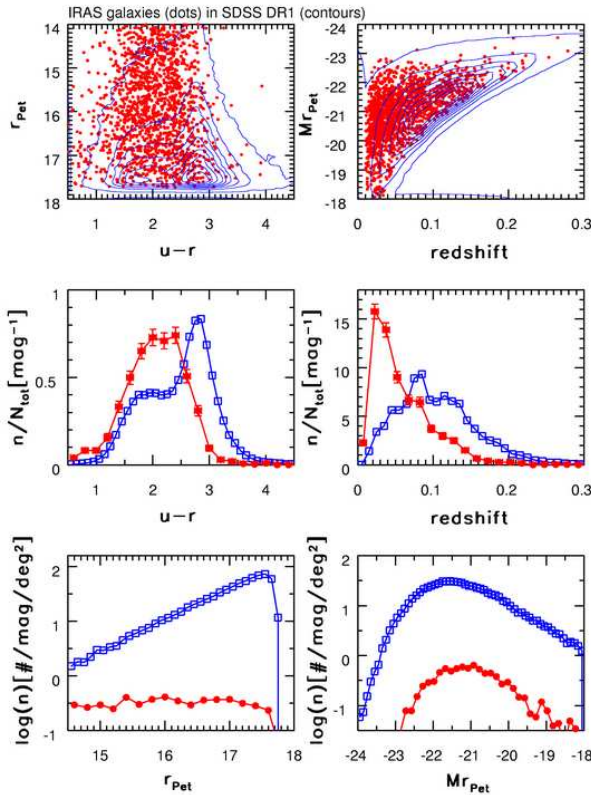
Figure 8. Analogous to Fig. 4, except that here galaxies listed in the IRAS FSC (dots, filled circles) are compared to the whole SDSS sample (contours, squares). Galaxies detected by IRAS are strongly biased towards blue galaxies and lower redshifts. The fraction of galaxies detected by IRAS decreases from 22% for $r_{Pet} = 14.5$ to 1% for $r_{Pet} = 17.5$.

The good agreement shows that predicted K-band flux is *not overestimated* for galaxies that are not in 2MASS XSC, and indicates that the proposed relations may be applicable for galaxies fainter than the 2MASS faint cutoff.

Given typical measurement errors in u, r, R_{50}^z and K, we conservatively conclude that the true astrophysical scatter of K-band magnitudes predicted from the blue part of the SED is not larger than $\sim$0.1 mag. Similarly, the relation $(J - K) = 2.172\,z_r + 0.966$, where z_r is redshift (see the bottom right panel in Fig. 5), predicts the $J - K$ measured by 2MASS with an rms scatter of 0.11 mag (0.07 mag at the bright end), and no significant residuals with respect to K, $u - r$, and redshift; that is, the rest-frame $J - K$ color distribution of *all* low-redshift galaxies is very narrow: $\sim$0.1 mag. These tight correlations demonstrate the remarkable one-dimensionality of galaxy spectral energy distributions from UV to IR wavelengths. We further discuss the spectral energy distribution of galaxies in Section 4.1, and an improvement to the K band flux prediction given by the eq. 1 in Section 4.4.

3.2 IRAS FSC

The distribution of SDSS galaxies detected by IRAS[7] in color-magnitude-redshift space is compared to the distribution of all SDSS galaxies in Fig. 8. The requirement that a galaxy is detected by IRAS introduces a strong bias towards optically blue galaxies and lower redshift (the middle two panels). The majority of these galaxies have emission lines and include both star-forming and AGN galaxies, as we discuss in more detail in Section 4.2. The completeness of the IRAS FSC catalog depends strongly on r_{Pet}, and varies from 22% for $r_{Pet} \sim 14.5$ to 1% for $r_{Pet} \sim 17.5$.

3.2.1 The correlation between $u - m_{60}$ and galaxy dust content

Interstellar dust absorbs UV and optical radiation and re-emits it at mid- and far-IR wavelengths. Hence, some degree of correlation is expected between the far-IR-optical/UV colors and the amount of dust in a galaxy.

Kauffmann et al. (2003a) used the distribution of galaxies in the plane spanned by the strength of the H_δ line and the 4000 Å break (D_{4000}) to obtain model-dependent estimates of stellar masses and dust content for SDSS galaxies. Given the position of a galaxy in the H_δ–D_{4000} plane, the most probable mass-to-light ratio is drawn from a model library. With the measured luminosity, this ratio then yields stellar mass. The observed luminosity is corrected for the dust extinction determined by comparing observed imaging $g - r$ and $r - i$ colors to model-predicted colors (the latter do not include the effects of dust reddening). The reddening correction needed to make models agree with data is interpreted as an effective optical depth in the SDSS z-band, A_z, due to a galaxy's interstellar dust. Here we find, using the measured properties of galaxies detected by IRAS, *independent* support for the notion that these model-dependent estimates of A_z are indeed related to the galaxy dust content.
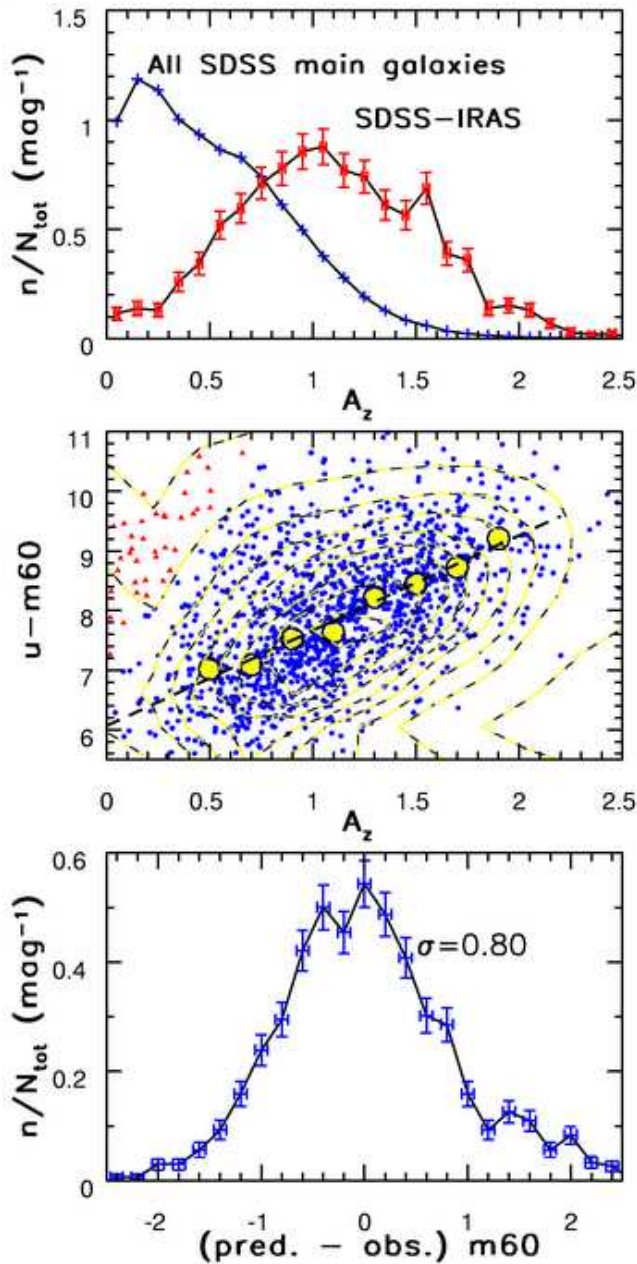
The top panel in Fig. 9 compares the distributions of A_z, determined by Kauffmann et al. (2003a), for all SDSS galaxies (pluses) and for the subset detected by IRAS (squares with error bars). Galaxies detected by IRAS have systematically higher values of A_z than the full SDSS "main" galaxy sample. If values of A_z, determined using *only* SDSS data, were not related to the dust content, there would be no systematic difference induced by requiring a detection by the fully *independent* IRAS survey.

Furthermore, we find a correlation between $u - m_{60}$ color (m_λ are IRAS measurements expressed as AB magnitudes, with λ=12, 25, 60, and 100 μm) and A_z. The small symbols in the middle panel in Fig. 9 show $u - m_{60}$ color as a function of A_z for 1200 highly probable SDSS-IRAS identifications, selected from the full SDSS-IRAS sample by limiting the maximum SDSS-IRAS distance to 20 arcsec. We first determine median values of $u - m_{60}$ in A_z bins of range 0.4–2.0, and then fit a linear relation to obtain

$$u - m_{60} = (6.0 \pm 0.2) + (1.64 \pm 0.2)\,A_z. \tag{2}$$

---

[7] We analyze the sources listed in the IRAS FSC catalog; see Appendix A5 for more details.

Figure 9. The top panel compares the distributions of the z-band dust extinction, A_z, inferred from SDSS spectra by Kauffmann et al. (2003a), for all SDSS galaxies (pluses) and for the subset detected by IRAS (squares with error bars). The middle panel shows the UV-far-IR color, $u - m_{60}$, as a function of A_z (both symbols and contours). The large symbols mark median values of $u - m_{60}$ in A_z bins in the 0.4–2.0 range. The dashed line is the best linear fit to these medians. The triangles, concentrated in the upper left corner, mark the $\sim$3% of galaxies that apparently do not follow this relation. The bottom panel shows the distribution of differences between the 60 μm flux measured by IRAS, and predicted values using the best-fit $u - m_{60}$ vs. A_z relation, and the u-band fluxes measured by SDSS. The rms of the distribution is marked in the panel (σ, in magnitudes).

We do not find significant differences in the best-fit relations fitted separately to AGN and star-forming subsamples (classified using emission-line strengths). The adopted A_z range excludes $\sim$3% of the sample that has very small A_z and $u - m_{60}$ about 2.5 mag redder than predicted by the above relation (triangles in the upper left corner in the middle panel in Fig. 8). It is not clear whether this 60μm excess is physical, or due to random matches. In any case, the fraction of the excluded sources is sufficiently small to have no effect on the overall correlation.

Using this relation and the measured SDSS u-band fluxes, we estimate the 60 μm flux, and compare it to the measured values in the bottom panel in Fig. 9. The IRAS 60 μm flux can be predicted within a factor of $\sim$2 (rms, or 0.8 mag) using *only* SDSS data. If, instead, the A_z estimates are ignored, and the 60 μm flux is estimated by assuming $u - m_{60} = 7.6$ (the median value) for all galaxies, the rms scatter between the predicted and measured values becomes 1.41 mag. Hence, the A_z estimates do contain information about the dust content.

We have also attempted to use the H_α/H_β line strength ratio as a proxy for effective dust extinction (e.g., see Moustakas, Kennicutt & Tremonti 2005, and references therein). The values of H_α/H_β and A_z determined by Kauffmann et al. (2003a) are well correlated. We find that H_α/H_β for emission-line galaxies can be determined from A_z with an rms scatter of 0.07 using the relationship

$$\frac{H_\alpha}{H_\beta} = 0.49 + 0.143 * A_z. \tag{3}$$

This relationship maintains its accuracy when only radio-selected, IR-selected, and subsamples separated into AGN and star-forming galaxies are considered. Thus, the $u - m_{60}$ vs. A_z and H_α/H_β vs. A_z correlations imply the existence of a $u - m_{60}$ vs. H_α/H_β correlation.

As expected, we find an overall correlation between $u - m_{60}$ and H_α/H_β ratio for SDSS-IRAS galaxies. However, it is not as strong as the $u - m_{60}$ vs. A_z relation discussed above. In terms of the rms scatter between predicted and measured 60 μm flux, it predicts 60 μm magnitude within 1.2 mag, that is, not as well as when using A_z. This implies that A_z values determined using SDSS spectra and sophisticated stellar population models may be a better estimator of effective dust content than the straightforward application of the H_α/H_β line-strength ratio.

Although it is hard to estimate the errors in IRAS flux measurements without an independent data set, the radio-IR correlation discussed in § 4.2.3 suggests that they are not larger than $\sim$0.4 mag, and therefore smaller than the rms scatter of 0.82 mag between predicted and measured 60 μm fluxes (the quoted formal IRAS FSC photometric errors are $\sim$0.2 mag). Thus, it may be possible to further improve the prediction for far-IR flux by using additional SDSS measurements such as sizes and UV/optical colors. For example, the differences between predicted and measured 60 μm fluxes are somewhat correlated with $u - r$ color: the median value is -0.1 mag for galaxies with $u - r < 2.22$ and 0.2 mag for redder galaxies. A similar effect is seen when the sample is separated into AGN and star-forming galaxies. We postpone such an analysis until the larger samples needed for robust quantitative multi-dimensional analysis are constructed.
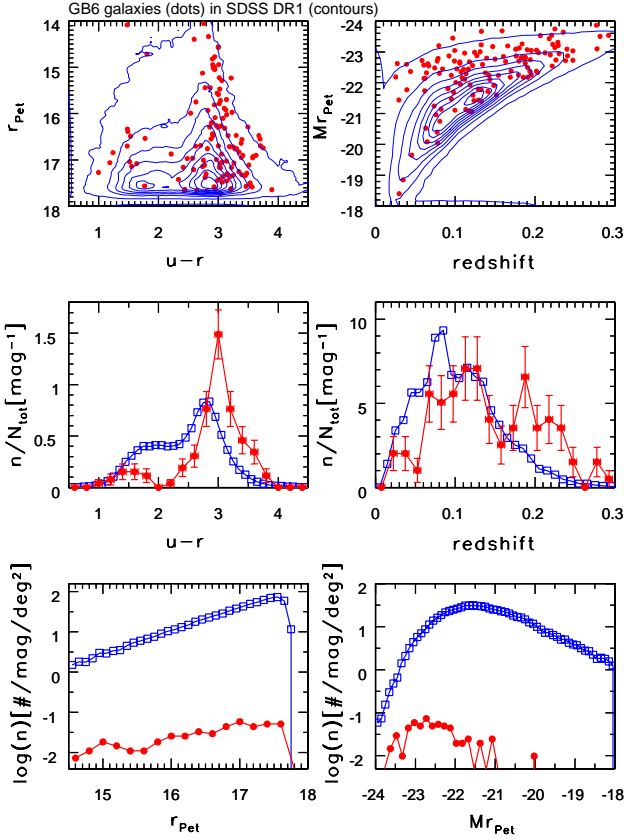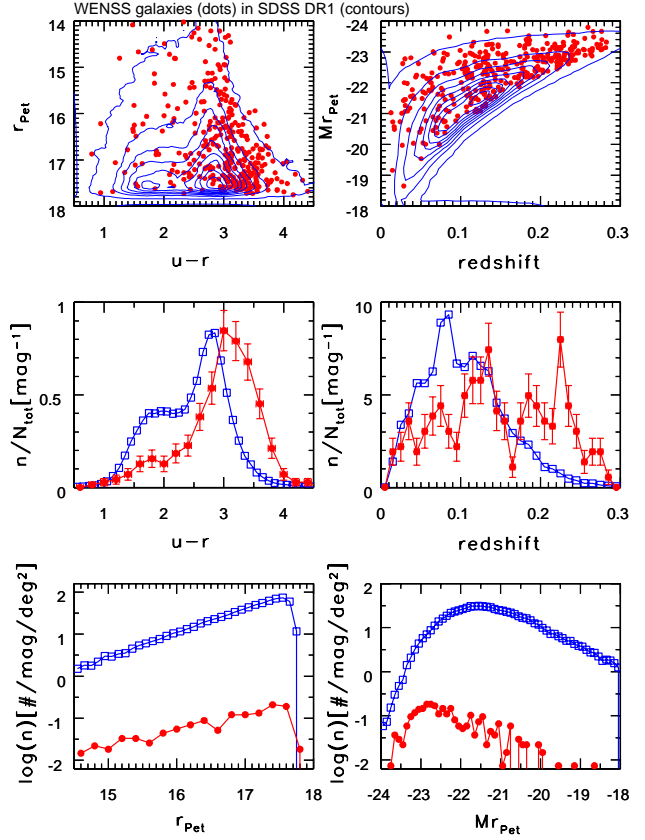
Figure 10. Analogous to Fig. 4, except that here galaxies detected by GB6 (dots, filled circles) are compared to the whole SDSS sample (contours, squares). Galaxies detected by GB6 are biased towards luminous red galaxies. The fraction of galaxies detected by GB6 is 0.22%.

Figure 11. Analogous to Fig. 4, except that here galaxies detected by WENSS (dots, filled circles) are compared to the whole SDSS sample (contours, squares). Galaxies detected by WENSS are biased towards luminous red galaxies. The fraction of galaxies detected by WENSS is 2.5%.

3.3 Radio surveys (GB6, FIRST, NVSS, WENSS)

The advent of modern sensitive large-area radio surveys (see Appendix A6 for brief descriptions and references), combined with an optical survey such as SDSS, offers significantly larger, more diverse, and accurate samples of radio sources with optical identifications than available until recently. Detailed studies of SDSS sources detected by the FIRST and NVSS 20 cm surveys was presented by Ivezić et al. (2002) and Best et al. (2005ab). Here we extend their analysis to multiwavelength radio observations by including data from the GB6 (6 cm) and WENSS (92 cm).

A summary of optical properties of SDSS galaxies detected by GB6 and WENSS is shown in Figs. 10 and 11. Analogous diagrams for galaxies detected by FIRST and NVSS can be found in Ivezić et al. (2002). The matching rate is the smallest for the GB6 catalog (0.22%, see Table 1), and the highest for FIRST (3.86%). The difference in matching fractions for the two 20 cm surveys (FIRST and NVSS) is due to their different faint flux limits and angular resolution. All four radio catalogs show similar distributions in color-magnitude-redshift space, despite the relatively large wavelength coverage and varying angular resolution. Radio galaxies are biased towards red, luminous galaxies and higher redshifts. Even when red galaxies ($u - r > 2.22$) are considered separately, their median $u - r$ color is redder by about 0.3

mag for the radio-detected subsample than for the whole red sample. However, this is simply a consequence of a bias in redshift induced by requiring radio-detection coupled with the K correction, as discussed by Ivezić et al. (2002). When compared in a small redshift range, *the radio-detected red galaxies have the same $u - r$ color distribution as red galaxies without radio detections.*

This sample is sufficiently large to test whether the radio spectral slope is correlated with optical properties, such as $u - r$. Using NVSS and WENSS measurements, we compute the radio spectral slope between 20 cm and 92 cm, and find no correlation with the $u - r$ color (see the top right panel in Fig. 12). We find that the distribution of this spectral slope for "main" SDSS galaxies is different from the distribution for the full multiwavelength radio sample (bottom right panel in Fig. 12); the latter have a larger fraction of sources with "steep" spectra ($\alpha \sim -1$). This difference is probably caused by distant radio-galaxies that are not present in the "main" SDSS sample, and by quasars. For further discussion of the distribution of galaxies and quasars in radio "color-color" diagrams, we refer the reader to Ivezić et al. (2004a).

We also analyzed the radio-to-optical flux ratio as a function of $u - r$. The top left panel in Fig. 12 shows the
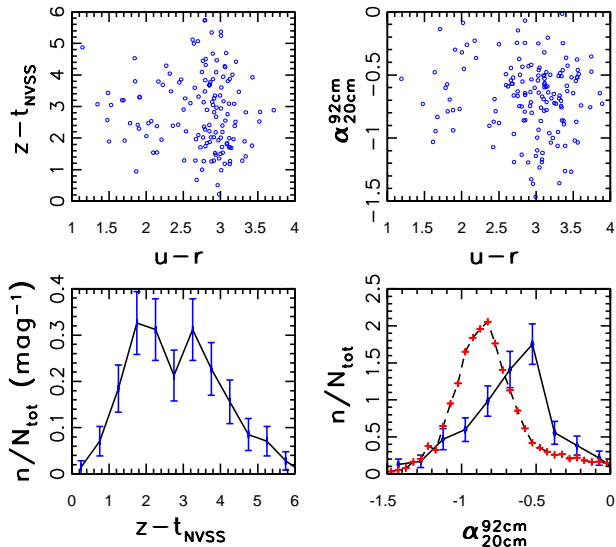
Figure 12. The top left panel shows the radio-optical color (20 cm and the z-band) vs. $u-r$ color for a subsample of these galaxies with redshift in the range $0.10 \leqslant z \leqslant 0.14$, and the bottom left panel shows the distribution of their radio-optical color. The top right panel shows the radio spectral slope (α for $F_\nu \propto \nu^\alpha$ between 20 cm and 92 cm) vs. $u-r$ color for SDSS galaxies detected by NVSS and WENSS surveys. The bottom right panel compares the distribution of the radio spectral slope for this sample (histogram with error bars) to the distribution of the radio spectral slope for all radio sources detected by the NVSS and WENSS surveys (histogram with pluses).

radio-optical color[8] $z-t_{NVSS}$ as a function of $u-r$ color for a subsample of SDSS-NVSS-WENSS galaxies with redshift in the range $0.10 \leqslant z \leqslant 0.14$. We use the z-band because the dependence of the bolometric correction for galaxies on color is the smallest in this band (see Section 4.1), and restrict the redshift range to minimize the effects of K correction. There is no discernible correlation between the radio-optical and $u-r$ color. However, the measured distribution of the radio-optical color, shown in the bottom left panel, is subject to numerous selection effects (such as multiple faint flux limits), and it is hard to uncover the intrinsic distribution without detailed simulations, which will be attempted elsewhere.

3.4 GALEX

The distribution of SDSS galaxies detected by GALEX[9] in color-magnitude-redshift space is compared to the distribution of all SDSS galaxies in Fig. 13. The requirement that a galaxy is detected by GALEX introduces a bias towards blue galaxies and lower redshift (the middle two panels). The

---

[8] Following Ivezić et al. 2002, we express all radio fluxes on AB magnitude scale. We would like to apologize to radio astronomers, as this seemed less of a problem than expressing SDSS and the UV-to-IR measurements in Janskys.
[9] We analyze sources listed in the GALEX Early Release Observations; see Appendix A3 for more details.
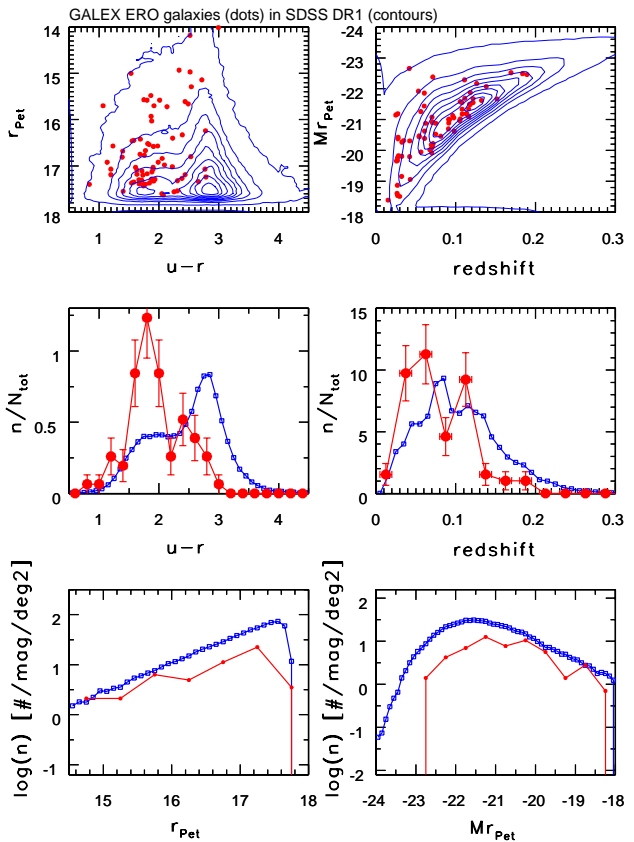
Figure 13. Analogous to Fig. 4, except that here galaxies detected by GALEX (dots, filled circles) are compared to the whole SDSS sample (contours, squares). Galaxies detected by GALEX are biased towards blue galaxies, and are dominated (70%) by emission line galaxies. The latter include both star-forming and AGN ($\sim$10%) galaxies (compare the middle left panel to Fig. 3). The fraction of SDSS "main" galaxies detected by GALEX is $\sim$42%, and approaches 100% at the bright end.
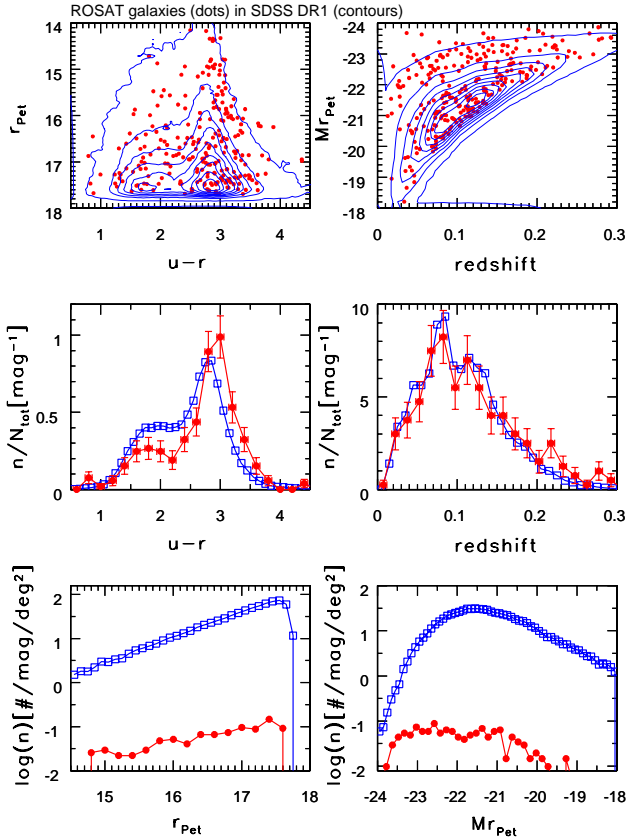
fraction of SDSS "main" galaxies detected by GALEX[10] is $\sim$42%, and approaches 100% at the bright end (the bottom left panel). The comparison of their $u-r$ distribution with those shown in Fig. 3 suggests that they are dominated by star-forming ($u-r \lesssim 2.2$) galaxies, but also include AGN ($2 < u-r < 3$) galaxies. The UV colors measured by GALEX support this conclusion (Agüeros et al. 2005). Furthermore, the majority (70%) of these galaxies have emission lines, and their distribution in the BPT diagram (discussed in more detail in Section 4.3) confirms that AGN emission, rather than starbursts, is the origin of UV flux in at least 10% of SDSS-GALEX galaxies.

3.5 ROSAT FSC

Matching ROSAT X-ray detections (including both hard and soft X-ray data) to SDSS DR1 optical counterparts produced a low (0.63%) matching fraction. Color-magnitude-redshift diagrams (Fig. 14) reveal a bias toward red galaxies,

---

[10] For an analysis of SDSS sources detected by GALEX that is not limited to SDSS "main" galaxies, we refer the reader to Agüeros et al. (2005) and references therein.

Figure 14. Analogous to Fig. 4, except that here galaxies detected by ROSAT (dots, filled circles) are compared to the whole SDSS sample (contours, squares). Galaxies detected by ROSAT are biased towards red luminous galaxies. The fraction of galaxies detected by ROSAT decreases from 0.6% for $r_{Pet} = 14.5$ to 0.2% for $r_{Pet} = 17.5$.

similar to that seen for radio surveys, but without a redshift bias. The small sample size prevents more detailed analysis. We refer the reader to Anderson et al. (2003) for an analysis of SDSS sources detected by ROSAT that is not limited to SDSS "main" galaxies.

4 PANCHROMATIC PROPERTIES OF SDSS GALAXIES

In this Section we combine the data from multiple surveys to construct and compare the UV-IR spectral energy distributions (SEDs) for various subsamples of galaxies, and analyze the changes in the BPT diagram induced by requiring detection at different wavelengths spanning the X-ray to radio range.

4.1 Dependence of colors on redshift and mean SEDs

The broad-band colors (SED) of a galaxy depend both on its type and redshift (K correction). The dependence of optical and infrared colors on redshift is illustrated in Fig. 15 for SDSS "main" galaxies listed in the 2MASS XSC and IRAS FSC. We used these diagrams to select a narrow redshift
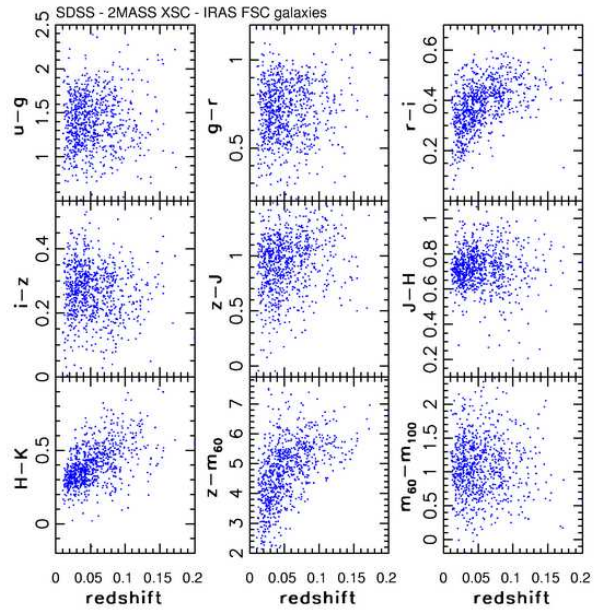
Figure 15. The dependence of optical and infrared colors on redshift for SDSS galaxies listed in 2MASS XSC and IRAS FSC catalogs. Colors are constructed with SDSS "model" magnitudes (AB system) and 2MASS XSC "default" magnitudes (Vega system). IRAS measurements at 60 μm and 100 μm are expressed on AB system (m_{60} and m_{100}).

range with a sufficient number of galaxies to construct the median SEDs for various subsamples (i.e., we use the median of each color to construct the overall SED). The median SEDs constructed with GALEX, SDSS, and 2MASS photometry for two subsamples of galaxies separated by $u - r$ color following Strateva et al. (2001) and with redshifts in the $0.03 \leqslant z \leqslant 0.05$ range (small enough that the colors are essentially rest-frame) are shown in the top panel in Fig. 16 (when constructing SEDs as a function of wavelength, we use Vega to AB conversion for 2MASS magnitudes from Finlator et al. 2000).

Galaxies with blue $u-r$ have all other colors, in the plotted wavelength range, bluer than galaxies with red $u - r$. Equivalently, the galaxy SEDs constructed with GALEX, SDSS, and 2MASS data are a nearly one parameter family (GALEX far-UV measurements do provide some additional information which cannot be extracted from SDSS and 2MASS broad-band measurements, see Agüeros et al. 2005). In particular, we demonstrated in Section 3.1.1 that the 2MASS K-band flux can be predicted within 0.2 mag using SDSS u and r fluxes. Smolčić et al. (2006) discuss an even tighter one-dimensional behavior of galaxies at wavelengths probed by SDSS.

The bottom panel in Fig. 16 shows the same SEDs as in the top panel, except that a linear scale is used instead of a logarithmic scale, and the SEDs are normalized by the bolometric flux. The bolometric flux is determined by integrating a spline fit to the 9 data points provided by GALEX, SDSS, and 2MASS, and using Rayleigh-Jeans extrapolation at wavelengths longer than 2.2 μm. The data values shown in the figure are also listed in Table 2.

The two normalized SEDs cross around the SDSS z

Table 2. The median UV-to-near-IR SEDs, normalized by the bolometric flux ($\nu F_\nu/F_{bol} \equiv \lambda F_\lambda/F_{bol}$), for blue ($u - r < 2.22$) and red ($u - r > 2.22$) galaxies with redshifts in the range $0.03 \leqslant z \leqslant 0.05$.

bandpass	$\lambda(\mu m)$	blue	red
f	0.15	0.08	<0.01
n	0.22	0.07	<0.02
u	0.35	0.24	0.07
g	0.48	0.42	0.27
r	0.63	0.53	0.45
i	0.77	0.59	0.53
z	0.93	0.58	0.58
J	1.25	0.55	0.57
H	1.65	0.49	0.53
K	2.17	0.34	0.38

band ($\sim$0.9 μm); showing that the dependence of the bolometric correction for galaxies on color in the SDSS photometric system is the smallest in the z-band. Hence, the flux measured in this band provides the best approximation to the bolometric flux (up to a constant; the important feature is the absence of color dependence). This band also has the smallest K correction for the redshifts probed by the SDSS "main" galaxy sample (since the SED slope is the smallest around this wavelength range), and is less sensitive to dust extinction than other SDSS bands. Thus, a good color-independent estimate of the bolometric flux (in the 0.2–2.2 μm wavelength range) can be simply obtained from the expression

$$(\nu\,F_\nu)_z = 0.58\,F_{\rm bol}, \tag{4}$$

or, equivalently,

$$L_{\rm bol} = 20.2\,10^{-0.4\,M_z}\,L_\odot, \tag{5}$$

where M_z is the absolute SDSS z-band magnitude. The uncertainty of these estimates is of order 5-10% (including calibration and SED integration errors, but not the individual z-magnitude measurement error, which can exceed 10% for faint galaxies).

We caution that the z-band should be used as a proxy for bolometric flux only for galaxies at redshifts $\lesssim 0.2$. For galaxies with larger redshifts the 2MASS J-band measurement should be used instead (and the H band for galaxies with redshifts beyond 0.6, though the number of such galaxies detected by 2MASS may be extremely small).

4.2 Do star-forming and AGN galaxies have different UV, IR, and radio properties?

In Section 2.1.2 we demonstrated that star-forming and AGN galaxies, classified using *only* emission-line strengths, have different broad-band optical properties such as $u - r$ and concentration index. Here we extend that analysis and compare their UV, IR, and radio properties.
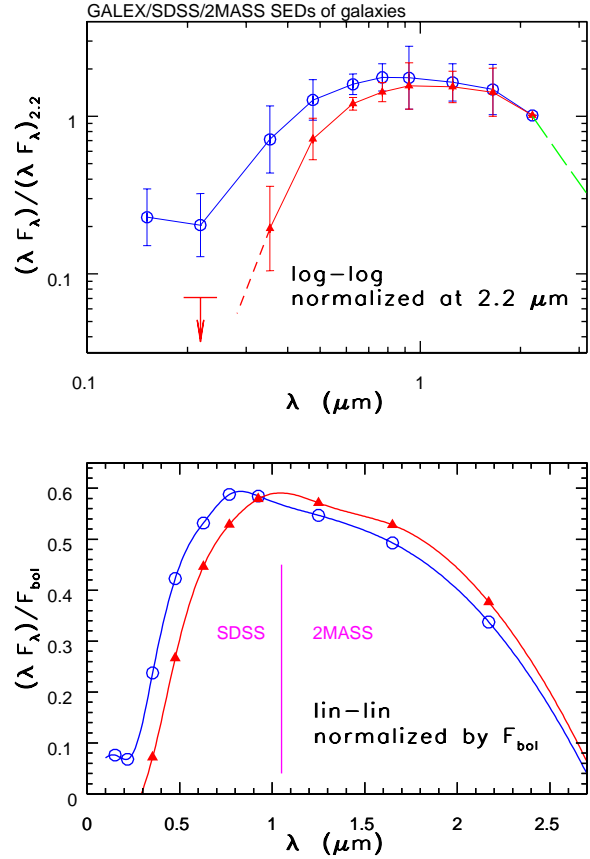
Figure 16. The top panel compares the UV-to-near-IR SEDs for blue ($u - r < 2.22$, circles) and red ($u - r > 2.22$, triangles) galaxies detected by the GALEX, SDSS, and 2MASS surveys, and with redshifts in the range $0.03 \leqslant z \leqslant 0.05$. The error bars indicate the root-mean-square color scatter (determined from the interquartile range). The data points are connected to guide the eye. The dashed line extending redwards from the K-band point (2.2 μm) is a Rayleigh-Jean extrapolation. The bottom panel shows the same data on a linear scale, normalized by the bolometric flux, with points connected by a spline fit. The dependence of the bolometric correction on color is the smallest in the SDSS z-band ($\sim$0.9 μm).

4.2.1 The UV-color difference between star-forming and AGN galaxies

The GALEX-SDSS sample discussed here is fairly small, and we only determined the median far-UV-to-near-UV colors[11], $f - n$ (f and n are AB magnitudes measured in the far- and near-UV GALEX bands), for the two classes. We find that star-forming galaxies are bluer (median $f - n$ is 0.1 ± 0.1) than AGNs (median $f - n$ is 0.5 ± 0.1). This is similar to the difference observed for $u - r$ (i.e., star-forming galaxies are bluer than AGNs). However, the analysis by Agüeros et

---

[11] For GALEX detections we require $n < 21$ or $f < 21$ and correct magnitudes for interstellar extinction using $A_f = 2.97A_r$ and $A_n = 3.23A_r$, where A_r is the r–band extinction from the maps of Schlegel, Finkbeiner & Davis (1998) distributed with SDSS data. These coefficients were evaluated using the standard interstellar extinction law from Cardelli, Clayton & Mathis (1989; M. Seibert, priv. comm.). The median A_r for the three AIS fields is 0.12, with a root–mean–square scatter of 0.02 mag.
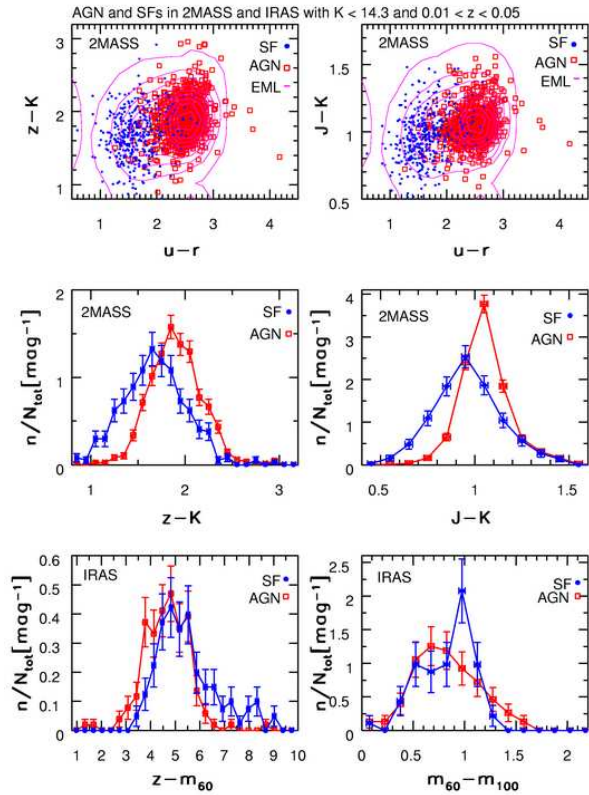
Figure 17. The comparison of optical and infrared colors for galaxies detected by SDSS, 2MASS, and IRAS surveys, in a restricted redshift range ($0.01 \leqslant z \leqslant 0.05$) to avoid K-correction effects. Star-forming galaxies (designated by "SF") show more far-IR emission, relative to optical/IR, than AGN galaxies, but bluer optical and near-IR colors.

al. (2005) suggests that the origin of the color differences is different for the $u-r$ and $f-n$ colors, because the latter are much more sensitive to the presence of starbursts and AGNs, while the $u-r$ color reflects the bolometrically dominant stellar population, as suggested by the analysis described in Section 3.1.1.

4.2.2 The IR-color difference between star-forming and AGN galaxies

In order to study differences in infrared properties between star-forming and AGN galaxies, we use the SDSS-2MASS and SDSS-IRAS samples, and restrict the redshift range to $0.01 < z < 0.05$ to avoid K-correction effects (further discussed below). The distribution of these galaxies in various optical/infrared color-color diagrams is shown in Fig. 17. In general, for any combination of optical and near-IR bands, star-forming galaxies are bluer than AGNs. For example, the $z-K$ and $J-K$ mean colors differ by 0.2 and 0.1 mag, respectively. According to the Kolmogorov-Smirnov test (KS hereafter), these differences are highly statistically significant, as is easily discernible from the two middle panels. However, this relationship reverses when using far-IR bands; star-forming galaxies have *redder* $z-m_{60}$ colors by $\sim$1 mag than AGNs (the KS probability that the two subsamples are
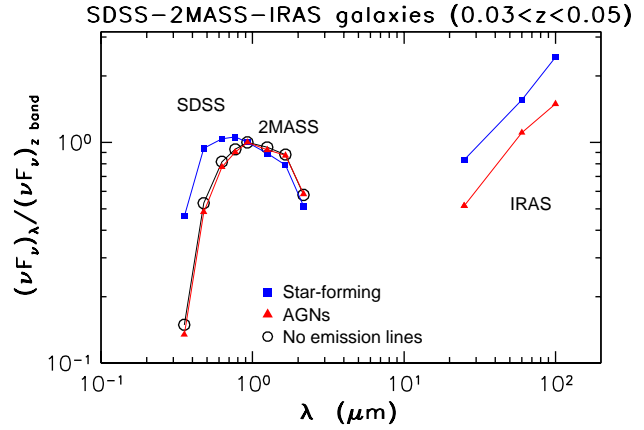
Figure 18. The optical-to-far-IR SEDs, normalized to the SDSS z-band, shown separately for galaxies without emission lines and AGN and star-forming emission-line galaxies detected by SDSS, 2MASS, and IRAS, and with redshifts in the $0.03 \leqslant z \leqslant 0.05$ range. Only the latter two subsamples have a sufficient number of IRAS detections to characterize the far-IR SED.

drawn from the same parent sample is $\sim 10^{-8}$) and have a much higher fraction of sources with $z - m_{60} \gtrsim 6$ (see the bottom left panel). This reversal is illustrated in Fig. 18 which compares the optical-to-far-IR SEDs, normalized to the SDSS z-band, for star-forming and AGN galaxies selected from a narrow redshift range. Since the z-band flux is a good measure of the 0.2 - 2.2 μm bolometric luminosity, this implies that star-forming galaxies emit more IR radiation as a fraction of their 0.2–2.2 μm bolometric output, than do AGN galaxies. This difference could be partially caused by a selection effect; since the apparent z-band magnitudes of star-forming galaxies tend to be somewhat fainter that those of AGN galaxies due to differences in luminosity functions and sampled redshift range, they will be detected by IRAS with the same probability only if they have somewhat redder $z - m_{60}$ colors. However, this effect does not seem to be quantitatively sufficient to explain the observed difference in median $z - m_{60}$ colors.

There are several plausible explanations for the different median $z - m_{60}$ colors for AGN and star-forming galaxies: star-forming galaxies could have warmer dust, significantly more dust, or more UV radiation that is absorbed by dust and re-emitted in the far-IR[12] than AGN galaxies (of course, these possibilities are not mutually exclusive). Different dust temperatures is probably ruled out two types have very similar $m_{60} - m_{100}$ color distributions; this color is much more sensitive to dust temperature than to the amount of dust; for a detailed discussion see e.g., Ivezić & Elitzur 1997), as shown in the bottom right panel in Fig. 17. In order to test the hypothesis that the difference is caused by a different amount of dust, we compared the distributions of extinction estimates, A_z, discussed in Section 3.2.1. As discernible from

---

[12] The observed difference could also be due to different dust optical properties, i.e., different ratio of far-IR to UV/optical opacity. While this possibility is not excluded by our analysis, it is not necessary in order to explain the observed trends. Similarly, we ignore the possible effects of dust geometry, e.g., the dust around AGN could have significantly different distribution than interstellar dust (e.g., Nenkova, Ivezić & Elitzur 2002).
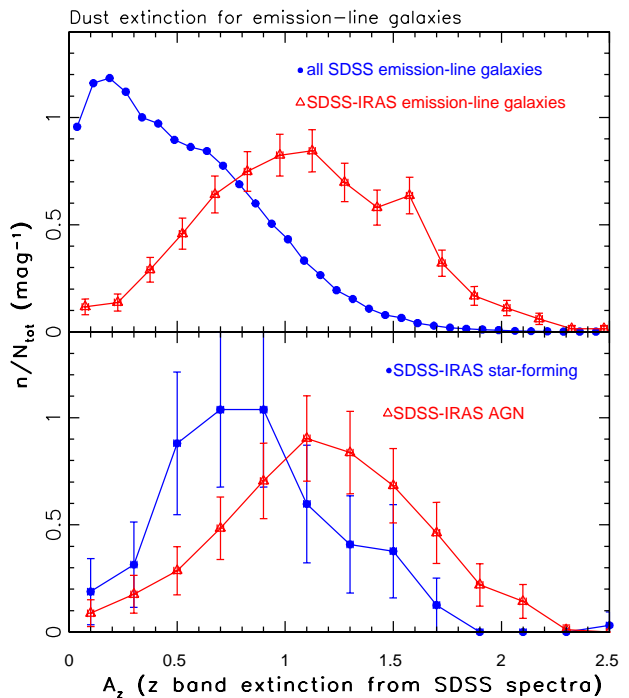
the bottom panel in Fig. 19, star-forming galaxies detected by IRAS typically have *smaller* A_z than AGN galaxies, thus ruling out this hypothesis.

Thus, it appears that star-forming galaxies emit more far-IR radiation (as a fraction of bolometric flux in the 0.2–2.2 μm wavelength range) than AGN galaxies, despite having smaller A_z of dust at similar temperatures, because they have significantly more UV radiation (again, as a fraction of bolometric flux in the 0.2–2.2 μm wavelength range) that is processed into far-IR wavelength range. This conclusion is supported by GALEX data discussed by Agüeros et al. (2005), who find a correlation between $f - n$ and contribution of the UV flux to the bolometric flux. Since star-forming galaxies tend to have bluer $f - n$ colors than AGNs (see Section 4.2.1), this implies that their UV flux contributes more to the bolometric flux than for AGN galaxies. Indeed, once a larger SDSS-GALEX-IRAS sample is available, the expected strong correlation between $f - m_{60}$ and A_z (similar to, and perhaps stronger than, the correlation shown in Fig 9) can be directly tested[13].

In a recent paper based on similar data, Pasquali, Kauffmann & Heckman (2005, hereafter PKH) found that the "AGN exhibit a significant excess in far-IR emission relative to star-forming galaxies", which apparently contradicts the results presented here. However, it should be pointed out that here we discuss the amount of IR radiation (at 60 μm) as a fraction of bolometric output in the 0.2–2.2 μm range (i.e., $z - m_{60}$ color), while PKH discuss the IR luminosity *per unit stellar mass*. Furthermore, their statement is valid for carefully selected pairs of AGN and star-forming galaxies that have similar physical characteristics such as stellar mass, color, size, etc. (it is also noteworthy that the distributions of stellar mass and stellar mass-to-light ratio are very different for AGN and star-forming galaxies, as shown by Kauffmann et al. 2003a). Hence, these are two independent, rather than contradictory, findings.

4.2.3 The radio-IR correlation

The large number of SDSS-IRAS-NVSS emission-line galaxies allows us to examine whether the well-known narrow distribution of the far-IR-to-radio flux ratio (van der Kruit 1971) is the same for (optically classified) star-forming and AGN galaxies. This correlation was interpreted by Helou et al. (1985) as a consequence of coupling between infrared thermal dust emission and radio non-thermal synchrotron emission, and it is not known whether the details of this coupling are the same for star-forming and AGN galaxies (e.g., see Bell 2003). In addition, both far-IR and radio emission are used as probes for ongoing and recent star formation (Hopkins et al. 2003 and references therein), and thus a ro-
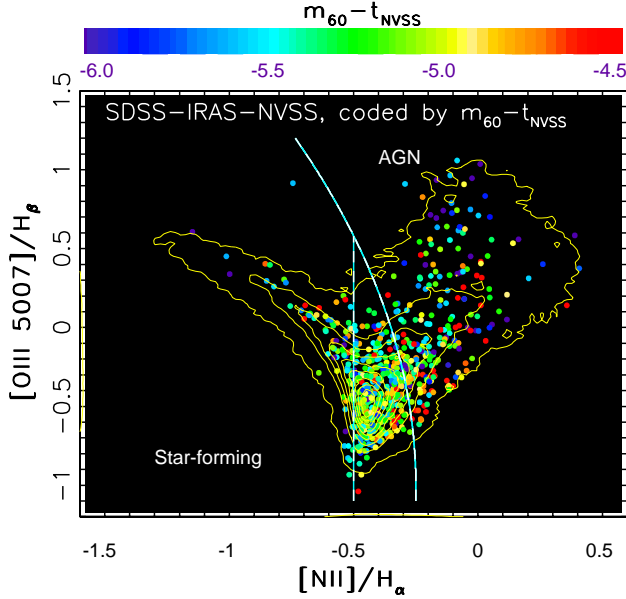
[13] The analysis of Buat et al. (2004) appears to support this expectation: they find that interstellar extinction for a far-IR flux-limited sample is higher than for a UV flux-limited sample. However, their estimates of interstellar extinction are derived from the UV-IR colors (rather than from independent data), and thus are strongly correlated with the sample flux limits. That is, the same effect would be obtained even if there were no correlation between the amount of dust in a galaxy and the UV-IR colors, and hence their analysis *cannot* be used to support our interpretation.

Figure 19. The top panel compares the z-band dust extinction inferred from SDSS spectra by Kauffmann et al. (2003a), A_z, for all SDSS emission-line galaxies (dots) and for those also detected by IRAS (triangles; analogous to the top panel in Fig. 9, which also includes galaxies without emission lines). The bottom panel compares the A_z distributions for AGN (triangles) and star-forming galaxies (dots) detected by IRAS. Note that star-forming galaxies detected by IRAS typically have *smaller* A_z than AGN galaxies.
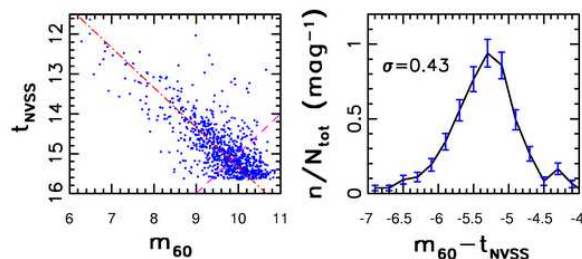
Figure 20. The left panel shows the radio 20 cm magnitude measured by NVSS as a function of 60 μ flux measured by IRAS, for 948 SDSS galaxies with a counterpart in IRAS FSC within 30 arcsec and in the NVSS catalog within 15 arcsec. The right panel shows the distribution of far-IR-radio color, $m_{60} - t_{NVSS}$, for 568 galaxies with $m_{60} + t_{NVSS} < 25$ (upper left region, away from the dashed line, shown in the left panel). The median value of $m_{60} - t_{NVSS}$ (-5.31) is shown as the diagonal dot-dashed line in the left panel, and the rms distribution width determined from the interquartile range is marked in the right panel.

Figure 21. The distributions of SDSS-IRAS-NVSS emission-line galaxies (dots) and all SDSS emission-line galaxies (contours) in the BPT diagram. The dots are colored according to their $m_{60} - t_{NVSS}$ color, as shown in the legend on top. *Both* AGN and star-forming galaxies are found in this sample, and they all follow the well-known radio-IR correlation.

bust measurement of this correlation is important for the comparison of studies based on different data sets.

The left panel in Fig. 20 shows the radio 20 cm magnitude measured by the NVSS as a function of 60 μm magnitude measured by IRAS for 948 SDSS "main" galaxies with a counterpart in IRAS FSC within 30 arcsec, and in the NVSS catalog within 15 arcsec. The strong correlation between the two fluxes[14] is evident. Only about 1% of sources have anomalously bright radio emission (by about $\sim$2 mag), a fraction that is consistent with contamination by random associations (the same fractions of AGN and star-forming galaxies are found among those 1% of sources, as in the whole sample; they are all bright point sources at 20 cm), but could also be due to radio-loud objects. In order to avoid the effect of faint flux limits on the distribution of the far-IR-to-radio flux ratio (i.e., the $m_{60} - t_{NVSS}$ color), we restrict the sample to 568 galaxies with $m_{60} + t_{NVSS} < 25$ (a condition perpendicular to the $m_{60} - t_{NVSS} = const.$ lines in the t_{NVSS} vs. m_{60} plane, see the dashed line in the left panel in Fig. 20), and show the distribution of the $m_{60} - t_{NVSS}$ color in the right panel. The median value of the $m_{60} - t_{NVSS}$ color is -5.31$\pm$0.02 (statistical errors only), with an equivalent Gaussian width (determined from interquartile range) of 0.43 mag. Such a narrow width is quite remarkable given so different wavelengths and survey technologies, and represents a strong constraint for the theories of coupled radiation mechanisms (e.g., Helou et al. 1985). It also places an upper limit of 0.4 mag on the IRAS photometric error for galaxies.

---

[14] Sometimes this correlation is shown in the luminosity vs. luminosity form, which boosts the impression of correlation strength. However, this is not a good practice since even uncorrelated measurements could give such an impression if the redshift distribution is sufficiently broad.

A very similar analysis of IR-radio correlation based on a smaller sample (176 UGC galaxies) was presented by Condon & Broderick (1988), who used a slightly different parameter $u = -0.4(m_{60} - t_{NVSS})$ (sometimes also called the q parameter, e.g., Bell 2003). They find a peaked distribution similar to that shown in Fig. 20, with 63 galaxies in the peak. The position of that peak corresponds to $m_{60} - t_{NVSS} = -5.05 \pm 0.05$, in good agreement with our analysis based on a $\sim$10 times larger sample. The width of the $m_{60} - t_{NVSS}$ distribution determined here (0.43 mag) corresponds to a width of 0.17 for the u (or q) distribution, somewhat smaller than $\sim$0.26 obtained in previous studies (e.g., Yun, Reddy & Condon 2001, Bell 2003). Condon & Broderick proposed that galaxies in this peak ($m_{60} - t_{NVSS} < -4$) are dominated by starbursts, while AGNs ("monsters" in their terminology) have too weak IR emission to be detected by IRAS, implying $m_{60} - t_{NVSS} > -4$.

The high-quality SDSS spectra and corresponding BPT-diagram based separation of emission-line galaxies into AGN and star-forming galaxies allows us to examine IR-radio correlation in detail. We find that over 1/3 of SDSS-NVSS-IRAS galaxies with emission lines can be reliably classified as an AGN based on their position in the BPT diagram, with an additional 50% in the transition region ("unknown" sources, using classification described in Section 2.1.2). That is, in addition to star-forming galaxies, optically-classified AGN galaxies also follow the tight IR-radio correlation. Hence, not all the "monsters" are confined to $m_{60} - t_{NVSS} > -4$ (assuming that they are correctly recognized by BPT analysis).

We note that the AGN/star-forming galaxy separation in the BPT diagram adopted here is fairly conservative (see Section 2.1.2). Figure 21 demonstrates that the majority of SDSS-IRAS-NVSS emission-line galaxies have ambiguous classification in the BPT diagram. However, it is easily discernible that a substantial fraction of these galaxies have optical emission-line strength ratios fully consistent with an AGN classification. The figure also shows that the position of a galaxy in the BPT diagram and the $m_{60} - t_{NVSS}$ color do not appear to be correlated. Visual inspection of SDSS g, r, i color composite images convincingly shows that *both* AGN and star-forming subsamples are dominated by galaxies with spiral morphology, as already pointed out by Condon & Broderick (1988). About half of them show disturbed morphology and nearby companions.

Using classification based on the BPT diagram, we compute and compare the slope of IR-radio correlation separately for AGN and star-forming galaxies. Two subsamples with 128 AGN and 46 star-forming galaxies yield median $m_{60} - t_{NVSS}$ values of -5.35 ± 0.05 and -5.14 ± 0.05, and widths of 0.61 and 0.38 mag, respectively[15]. The difference between the medians is $\sim 3\sigma$ significant, and suggests that the details of radiation coupling mechanisms may be different for star-forming and AGN galaxies (i.e., among galaxies

---

[15] The $m_{60} - t_{NVSS}$ color measurement should not be interpreted as implying a power-law spectral energy distribution between 60 μm and 20 cm with the power-law index of $\sim$0.6 ($F_\nu \propto \nu^\alpha$). For example, galaxies have $\alpha \sim -0.5$ between 6 and 20 cm (Ivezić et al. 2004a), and $m_{60} - m_{100} \sim 1$, implying $\alpha \gtrsim 1$ between 100 μm and 6 cm, that is, a steeper decrease of flux with wavelength, than implied by the $m_{60} - t_{NVSS}$ colors.
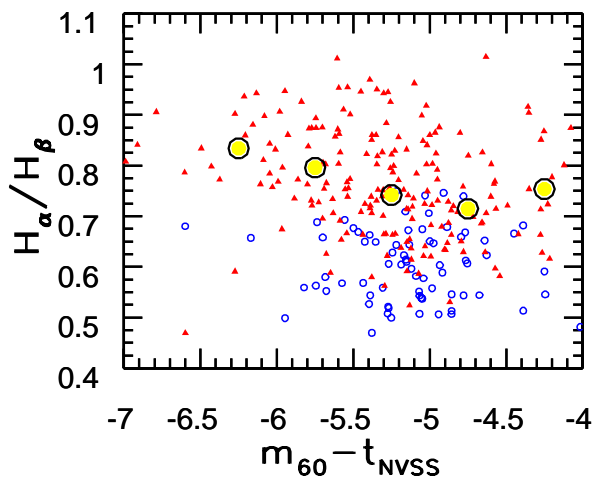
Figure 22. The distribution of AGN and star-forming galaxies in the radio-IR color, $m_{60} - t_{NVSS}$, vs. optical emission-line strength ratio, H_α/H_β. Small blue circles show star-forming galaxies and red triangles AGN galaxies. The large circles are the median values of H_α/H_β in narrow $m_{60} - t_{NVSS}$ bins for AGN galaxies, and demonstrate that the strength of IR emission for AGN galaxies, relative to their radio emission, increases with the H_α/H_β line strength ratio.
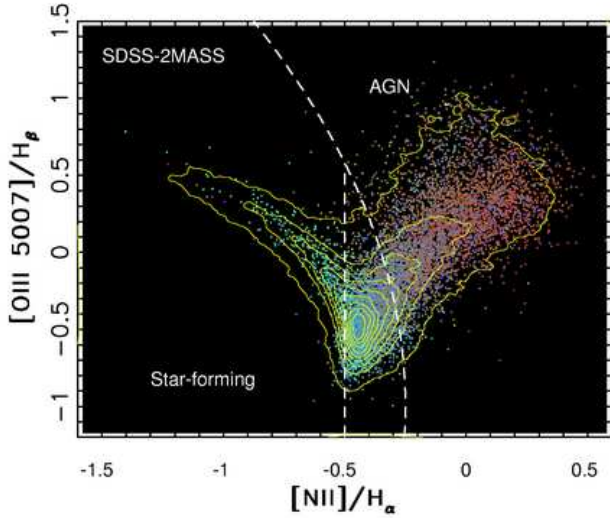

Figure 23. The distributions of SDSS-IRAS-NVSS emission-line galaxies (dots) and all SDSS emission-line galaxies (contours) in the BPT diagram. The dots are colored according to their H_α/H_β line strength ratio, as shown in the legend on top. Note that objects with the largest values of H_α/H_β ratio (red) are found almost exclusively in AGN region.

that follow IR-radio correlation, star-forming galaxies appear to show ~20% more radio emission, relative to far-IR, than AGN galaxies). We note that this result should be considered somewhat tentative because there may be systematic effects that are not included when estimating uncertainties in the medians[16], and thus its significance could be overestimated. It is also noteworthy that none of star-forming galaxies have $m_{60} - t_{NVSS} > -4$, while this is true for 4% of AGNs (that is, an opposite trend than for medians).

We searched for possible correlations between $m_{60} - t_{NVSS}$ and other observables that could perhaps explain the different median values of this color for AGN and star-forming subsamples (either as selection effects, bad data, bad analysis method, or astrophysics). We analyzed quantities such as colors, redshift, stellar mass, luminosity, angular size, dust extinction estimate A_z, etc., and the only quantity that appears to have an effect on $m_{60} - t_{NVSS}$ is the H_α/H_β ratio, as shown in Fig. 22 (see also Fig. 23 which illustrates correlation between the H_α/H_β ratio and the position in BPT diagram). Star-forming galaxies are confined to the $H_\alpha/H_\beta < 0.7$ region, while AGN galaxies span the whole observed range of H_α/H_β. Furthermore, as the H_α/H_β line strength ratio increases, the strength of IR emission for AGN galaxies, relative to radio emission, also increases (i.e., the $m_{60} - t_{NVSS}$ color becomes bluer). Since the measurement of $m_{60} - t_{NVSS}$ is fully independent of the H_α/H_β measurement, this behavior provides additional support for the 3σ significant difference in the slopes of IR-radio correlation

---

[16] Some of this difference could be due to systematically different radio morphology, an interesting possibility that is beyond the scope of this work. It is noteworthy that we did not find a correlation between the $m_{60} - t_{NVSS}$ color and the radio spectral slope between 20 cm and 92 cm.
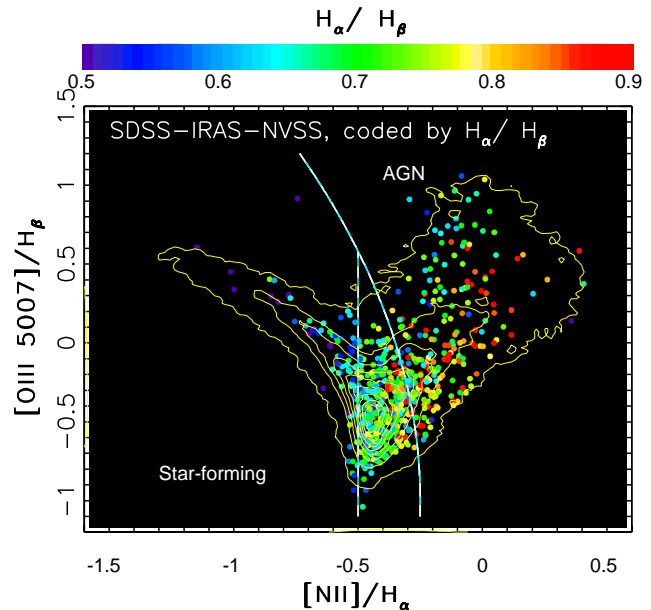
for star-forming and AGN galaxies (note, however, that the AGN presence could have an effect on the measured H_α/H_β ratio). It is noteworthy that there is no evidence for a similar behavior in the $m_{60} - t_{NVSS}$ vs A_z diagram, although some degree of correlation exists between H_α/H_β and A_z. This may mean that the effects of gas and dust on infrared and radio emission are more complex than implied by a simple linear IR-radio correlation (for a detailed discussion of this possibility see Bell 2003).

Given that both AGN and star-forming subsamples of SDSS-NVSS-IRAS galaxies follow very similar, if not identical, radio-IR correlation, it is interesting to investigate what fraction of the full SDSS-NVSS and SDSS-IRAS subsamples could follow this correlation (that is, galaxies that are detected by only two, instead of all three, surveys). We perform this analysis by using the observed radio-IR correlation to predict t_{NVSS} for SDSS-IRAS galaxies, or m_{60} for SDSS-NVSS galaxies. In the second step we select galaxies with predicted fluxes 1 mag brighter than the faint limit of the corresponding third catalog (to account for the scatter due to photometric errors), and then determine what fraction of these galaxies are actually detected. For example, if *every* IRAS galaxy follows IR-radio correlation, then we estimate that $> 90\%$ of SDSS-IRAS galaxies with predicted $t_{NVSS} < 15.5$ should be detected by NVSS. We find that indeed 92% of SDSS-IRAS galaxies with $t_{NVSS}^{predicted} = m_{60} + 5.3 < 14.5$ are detected by NVSS.

The converse is not true. Only about 1/3 of SDSS-NVSS *emission-line* galaxies with $m_{60}^{predicted} = t_{NVSS} - 5.3 < 9$ are detected by IRAS. This is consistent with a hypothesis that there is another source of radio emission, in addition to the component that is correlated with IR emission. The elevated radio emission is then responsible for the NVSS

Figure 24. The comparison of the distributions of SDSS-2MASS emission-line galaxies (dots) and all SDSS emission-line galaxies (contours) in the BPT diagram. The dots are colored according to their position in the concentration index vs. $u-r$ diagram, shown in the top right panel in Fig. 2. The AGN-to-SF number ratio for SDSS-2MASS galaxies is 10.1, while it is 1.6 for the whole SDSS sample.

detection, but IR emission is too weak for an IRAS detection. Presumably, those AGNs that are detected by both NVSS and IRAS are mostly radio-quiet, while those with elevated radio emission are mostly radio-loud. Not surprisingly, SDSS-NVSS emission-line galaxies without IRAS detection have typically redder $u-r$ colors than those detected by both NVSS and IRAS (the difference in medians is 0.6 mag). The detection fraction by IRAS is different for AGN and star-forming subsamples of SDSS-NVSS sample: while 50% of star-forming SDSS-NVSS galaxies are detected by IRAS, this is true for only 20% of AGNs (for galaxies with $m_{60}^{predicted} < 9$). These statistics indicate that the *majority* (80%) of emission-line galaxies classified *optically* as AGNs emit more flux at radio wavelengths than implied by their IR fluxes and the mean IR-radio correlation. Again, practically all of those remaining 20% AGNs from SDSS-NVSS subsample that are also detected by IRAS do follow a very tight IR-radio correlation.

4.3　Adding panchromatic information to the BPT diagram

In preceding Sections we have discussed the broad-band panchromatic properties of galaxy samples selected by their emission-line properties with the aid of the BPT diagram (see Section 2.1.2). In this Section we study how the morphology of galaxy distribution in the BPT diagram changes when requiring detections at other wavelengths (see Figs.24 to 28).

　　The AGN-to-star-forming galaxy number ratio is 1.6 for the whole SDSS sample. Although we exclude a large number of galaxies with uncertain classification (see Section 2.1.2), this ratio is a good relative measure of the
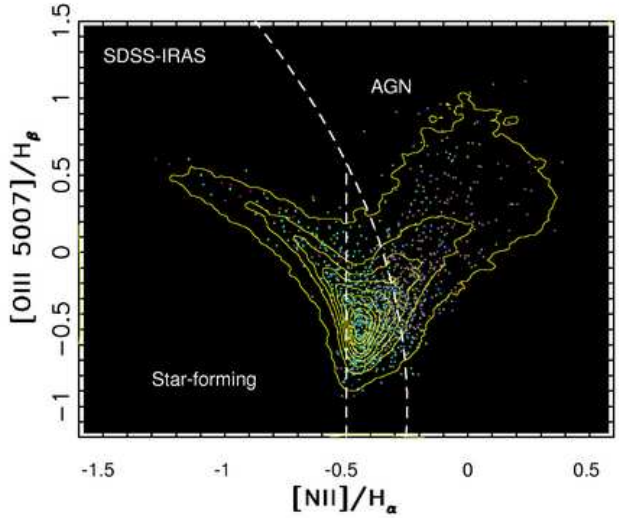
Figure 25. Analogous to Fig. 24, except for SDSS-IRAS galaxies. The AGN-to-SF number ratio for SDSS-IRAS galaxies is 2.7.
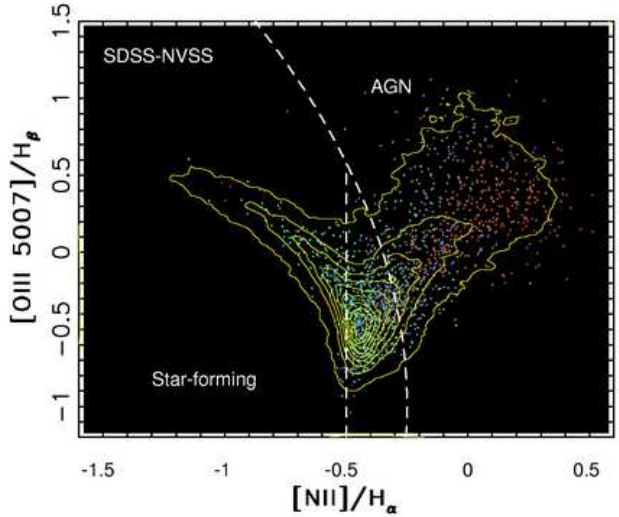
Figure 26. Analogous to Fig. 24, except for SDSS-NVSS galaxies. The AGN-to-SF number ratio for SDSS-NVSS galaxies is 4.7.

changes in the BPT diagram[17]. We find that the AGN-to-star-forming galaxy number ratio is systematically larger for subsamples with detection at other wavelengths, except for SDSS-GALEX sample, and it is the largest for SDSS-2MASS sample (10.1). Such a high ratio for SDSS-2MASS sample is a consequence of fairly bright K-band flux limit, and the fact that AGN galaxies have redder optical-to-near-IR SEDs than star-forming galaxies.

---

[17] Note that the AGN-to-star-forming galaxy number ratio depends on the adopted cutoff for the emission line detection significance. Higher values than the 3σ adopted here (see Section 2.1.2) would result in a lower AGN-to-star-forming galaxy number ratio because many AGNs are very weak-lined LINERs (Heckman et al. 2004).

Figure 29. *g, r, i* composite SDSS images of SDSS-GALEX galaxies randomly chosen from three subsamples classified using emission-line strengths measured from SDSS spectra (Kauffmann et al. 2003a). The first row shows images of star–forming galaxies, the second of AGN; and galaxies in the third row have uncertain classifications. North is up, and the images are roughly 25″ on a side.

The AGN-to-star-forming galaxy number ratio is the smallest for SDSS-GALEX sample (0.1, but it could be as high as 0.3 if the unclassified galaxies are dominated by AGN galaxies, see Fig. 28). The lower limit on this ratio is sufficiently high to exclude the possibility that SDSS-GALEX galaxies represent a clean sample of starburst galaxies. In order to present further evidence for this claim, we have visually inspected SDSS g, r, i color composite images of these galaxies (a total of 55) and found that the classification based on emission-line strengths is well correlated with morphology. SDSS images of random subsamples of AGN, star-forming, and unclassified galaxies are shown in Fig. 29. Clear morphological differences between galaxies classified as star-forming and as AGN are easily discernible, with the latter being more centrally concentrated. This further demonstrates that *at least some GALEX/SDSS galaxies are more likely to be AGN than star-forming.*

4.4 An improvement of the K band flux prediction

In Section 3.1.1 we showed that it is possible to estimate the K-band magnitude with a scatter as small as ∼0.2 mag using only SDSS data. In this Section we explore whether the residuals between predicted and 2MASS K-band magnitudes correlate with several model-dependent quantities

determined by Kauffmann et al. (2003a), and whether the residuals show the same behavior when AGN and star-forming galaxies are treated separately.

The strongest correlation between the K-band SDSS-2MASS residuals and another quantity is found for A_z, the galaxy dust content discussed in detail in Section 3.2.1. The top panel in Fig. 31 illustrates this correlation. A best straight line fit is given by

$$\Delta(r - K)^* = 0.213 \; A_z - 0.033 \qquad (6)$$

This correlation may be interpreted as the effect of dust on the observed r-band flux (however, note that the simple extinction screen approximation is probably not appropriate). When this correlation is subtracted from $(r - K)^*$ given by the eq. 1, the width of the residuals distribution decreases by a factor of 2, to 0.1 mag! In other words, given the $u - r$ color, redshift, and A_z determined using SDSS data, the 2MASS K-band measurements can be predicted with a scatter of only 0.1 mag. Most of this scatter can be attributed to the measurement errors. For example, assuming conservative lower limits for errors in $u-r$ (0.03 mag), K (0.03 mag, Jarrett et al. 2000), and R_{50}^z (2%), the expected scatter due to measurement errors is 0.09 mag. Hence, the observed residual scatter of 0.1 mag is likely dominated by measurement errors. We note that the final distribution of the $r - K$ residuals shown in the bottom panel in Fig. 30
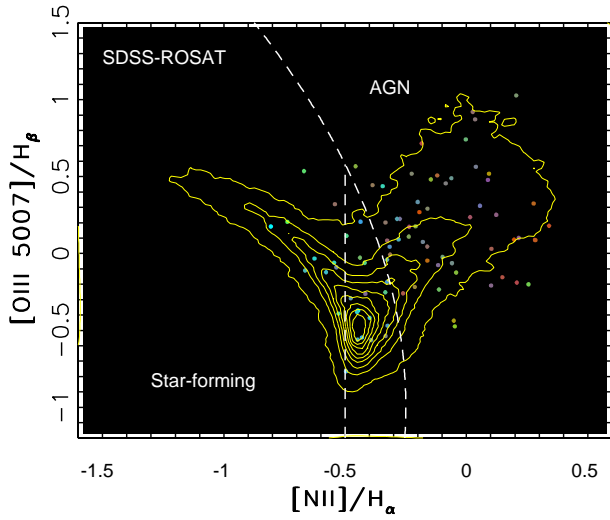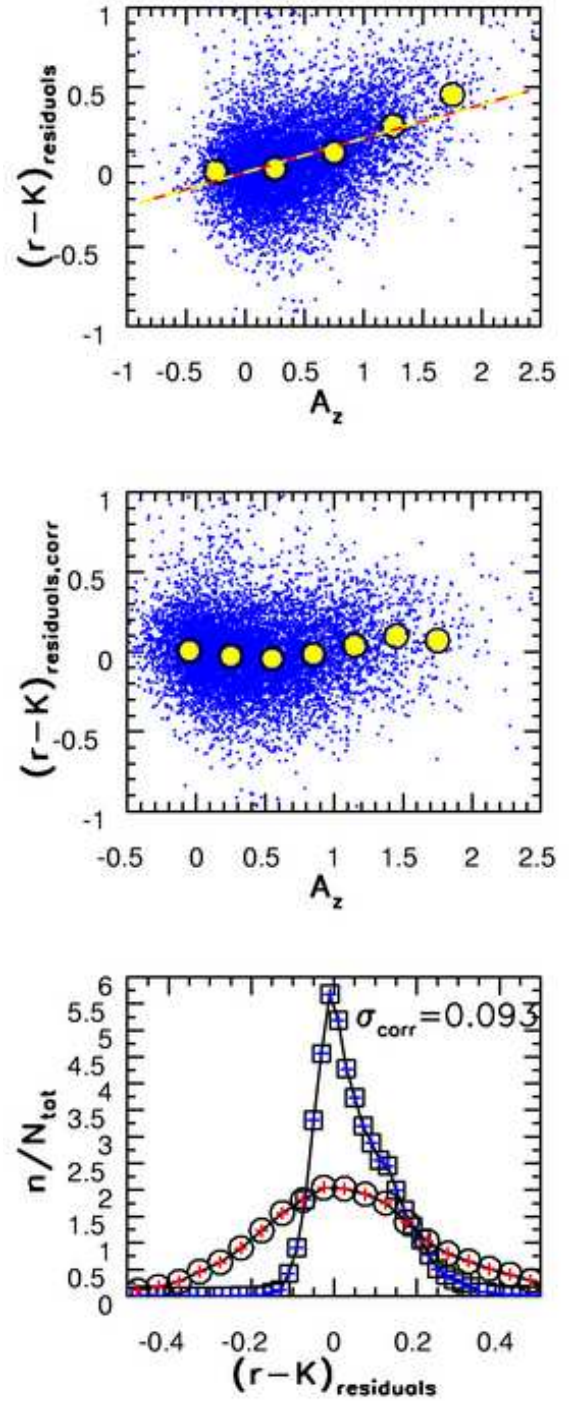
Figure 27. Analogous to Fig. 24, except for SDSS-ROSAT galaxies. The AGN-to-SF number ratio for SDSS-ROSAT galaxies is 5.7.
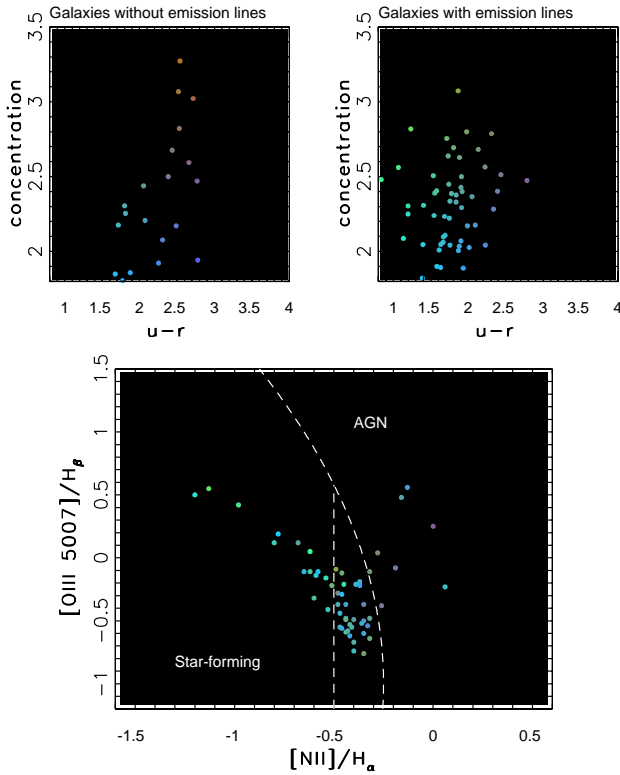

Figure 28. Analogous to Fig. 2, except for SDSS-GALEX galaxies. The lower limit on AGN-to-SF number ratio for SDSS-GALEX galaxies is at least 0.1, and it could be as high as 0.3.

Figure 30. The top panel shows the dependence of residuals between predicted and measured K-band magnitudes on the z-band dust extinction, A_z, inferred from SDSS spectra by Kauffmann et al. (2003a). Individual galaxies are shown by small symbols, and large circles show the median values in A_z bins. The best-fit straight line to these medians is also shown. The residuals corrected for this median trend are shown in the middle panel. The bottom panel compares the distributions of uncorrected residuals (circles) and the corrected ones (squares). The distribution width for the latter is only about one half of that for the former.
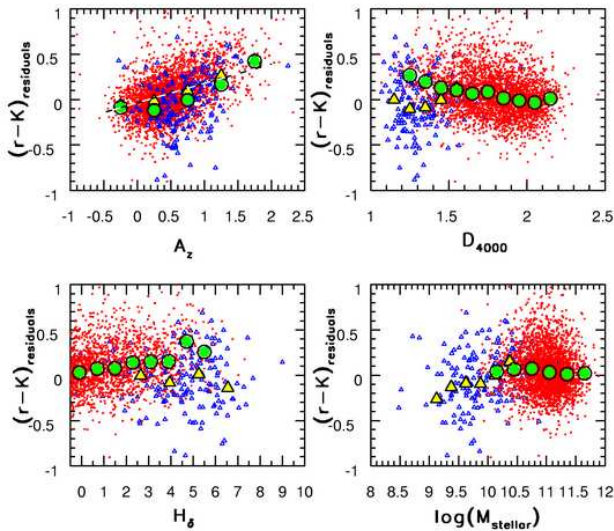
Figure 31. The top left panel is analogous to the top panel in Fig. 30, except that here AGN (dots and circles) and star-forming galaxies (small and large triangles) are treated separately. The straight line is the same line as in the top panel in Fig. 30. The other three panels are analogous to the top left panel, except that they show the dependence of residuals on the 4000 Å break (D_{4000}), the strength of H_δ line, and stellar mass.
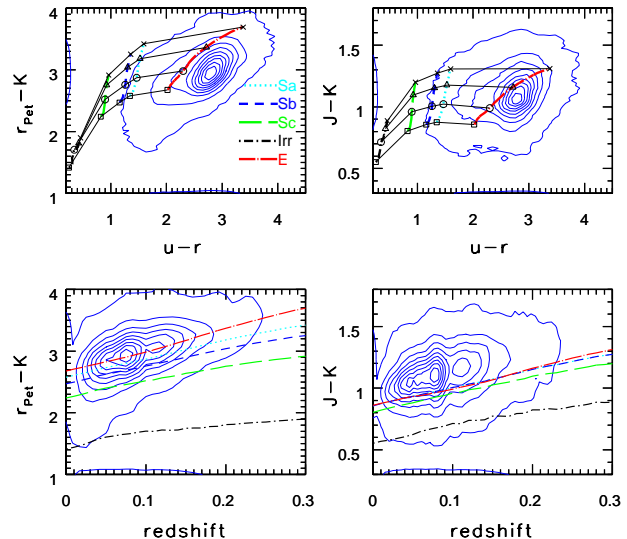

Figure 32. A comparison of the observed galaxy distribution (contours) in representative color-color and color-redshift diagrams and the Bruzual & Charlot (1993, 2003) model predictions. The SEDs for five representative synthetic galaxies are convolved with SDSS and 2MASS bandpasses for a grid of redshifts in the 0–0.3 range (thick lines). The positions along these lines that correspond to redshifts of 0, 0.1, 0.2 and 0.3 are marked by squares, circles, triangles and crosses, respectively, and are connected by thin lines.

is skewed. This could be due to the fact that the dependence of the $r - K$ residuals on A_z was fit by a straight line, while the data display some curvature. Also, it could be that there are two subpopulations of galaxies that have slightly different SEDs.

Since the residual astrophysical scatter is apparently much smaller than 0.1 mag, one is tempted to conclude that 2MASS measurements are not required to study SDSS galaxies. This would not be a valid conclusion for at least two reasons. First, the measurement error for 2MASS K band magnitudes is ~0.03 mag, which is smaller than the residual scatter for predicted K band magnitudes (0.1 mag). Second, we have not investigated morphological properties of galaxies in the near-IR, where smaller dust extinction could reveal features not visible in the optical wavelength range.

We have also studied the correlation between the K-band SDSS-2MASS residuals and the 4000 Å break (D_{4000}), the strength of H_δ line, and stellar mass (Fig. 31). None of the correlations is as strong as the correlation with A_z. As shown in Fig. 31, the overall behavior of AGN and star-forming subsamples are similar to each other, though not identical.

4.4.1 Comparison with Bruzual & Charlot models

Motivated by the surprisingly small residual scatter in the K band flux prediction (0.1 mag), we have investigated the Bruzual & Charlot (1993, 2003) model predictions for the distribution of optical and near-IR galaxy colors. The top left panel in Fig. 32 shows that for a given galaxy type, the $r - K$ color is a function of redshift, and at a given redshift the $r - K$ color is a function of galaxy type. This behavior is in agreement with observations, although model

galaxies have the $u - r$ colors too blue by several tenths of a magnitude. The models are also in agreement with a $J - K$ vs. redshift relation that is independent of galaxy type, as discussed in Section 3.1.1 (see top right panel).

The behavior of simple stellar populations (as opposed to synthetic galaxies) in the same diagrams suggests that both the $r - K$ and $J - K$ colors are sensitive to metallicity, with about 0.7 mag and 0.2 mag redward shifts in the $r - K$ and $J - K$ colors as the metallicity increases by a factor of 10. The observed small residual scatter in the K band flux prediction thus implies that the galaxy metallicity distribution is fairly narrow: about 0.2 dex around the median value. This is in agreement with Tremonti et al. (2004) who found a very tight mass-metallicity relation (0.1 dex metallicity scatter at a given mass).

5 SUMMARY AND DISCUSSION

This study indicates the enormous potential of modern massive sensitive large–scale surveys, and emphasizes the added value obtained by combining data from different wavelengths. While qualitatively our study is in agreement with previous work (e.g., galaxies detected by IRAS tend to be blue), the sample size and the wealth of measured parameters allowed us to obtain some qualitatively and quantitatively new results.

Galaxy SEDs form a nearly one-dimensional sequence in the optical-to-near-IR range. For example, the SDSS u and r-band data, supplemented with redshift and dust content estimate, can be used to predict K-band magnitudes measured by 2MASS with an rms scatter of only 0.1 mag and the intrinsic astrophysical scatter probably significantly

smaller. Within the restricted wavelength range probed by SDSS, this scatter is even smaller. Smolčić et al. (2006) show that the rest-frame $r - i$ color (5500–8500 Å wavelength range) can be predicted with an rms of only 0.05 mag using Strömgren colors evaluated in the 4000–5800 Å wavelength range. Smolčić et al. (2006) also find a strong correlation between Strömgren colors and the position of a galaxy in the BPT diagram, a result that is confirmed here using the $u - r$ color. As shown by Smolčić et al., other parameters, such as those determined by Kauffmann et al. (2003a), can also be used to parametrize the position of a galaxy on this one-dimensional sequence in the multi-dimensional color space. Or equivalently, using the terminology from Yip et al. (2004), most of the variance in galaxy SEDs is already absorbed in the first few principal components.

We integrate the broad-band UV-to-near-IR SEDs of dominant galaxy types and find that the z-band flux is the closest, color-independent, proxy for bolometric flux measurement in the 0.2–2.2 μm range for galaxies with redshifts smaller than ∼0.2.

We find that galaxies detected by GALEX include a non-negligible fraction (10-30%) of AGNs, and hence do not represent a clean sample of starburst galaxies. This conclusion is supported by their $u - r$ color distribution, position in the BPT diagram, and morphological appearance (see Agüeros et al. 2005 for more details).

We demonstrate that interstellar dust content inferred from optical spectra by Kauffmann et al. (2003a) is indeed higher for galaxies detected by IRAS confirming the reliability of the A_z measurement. This represents a dramatic *independent* support for the notion that these model-based *optical* estimates of A_z are related to the galaxy dust content. Furthermore, A_z can be used with the u-band measurements to predict IRAS 60 μm flux within a factor of ∼2, which suggests that the Bruzual & Charlot (1993, 2003) models used to derive A_z provide fairly good description of the relevant physics. Even more detailed and robust analysis along these lines will be possible with the advent of GALEX and Spitzer data.

We find that star-forming galaxies tend to be bluer than AGN galaxies for all photometric bands bluewards from the K-band, while they have redder far-IR-to-optical colors. We conclude that star-forming galaxies have redder far-IR-to-optical colors than AGN galaxies because they have more UV light that is processed to far-IR range, as a fraction of the 0.2–2.2 μm bolometric flux. We emphasize that a variety of different data for the *same* galaxy sample was required to reach this conclusion: GALEX, SDSS, 2MASS, and IRAS photometry, as well as the interstellar dust content inferred from SDSS optical spectra with the aid of sophisticated models.

A large sample of galaxies that have SDSS spectra and are detected by IRAS and NVSS allowed us to study the IR-radio correlation separately for star-forming and AGN galaxies. We confirm that both galaxy types follow a tight correlation, and find that a large fraction (80%) of optically classified SDSS-NVSS AGN galaxies show significantly more radio emission than expected from their IR flux (technically, we show that IR fluxes predicted from observed radio emission for galaxies that are not detected by IRAS are higher than the corresponding IRAS upper flux limits, see Section 4.2.3). We also find marginal evidence for different slopes of IR-radio correlation for AGN and star-forming subsamples, an effect that seems to be related to the H_α/H_β line strength ratio.

Perhaps the most important conclusion of our study is that little more than a single datum can be learned about galaxies from photometric data whose accuracy is not demonstrably better than ∼0.1 mag. Fortunately, all three major modern galaxy surveys, GALEX, SDSS, and 2MASS, appear to have achieved this goal and, together with surveys such as FIRST and NVSS, opened unprecedented opportunities for detailed studies of galaxies.

REFERENCES

Abazajian, K., Adelman, J.K., Agüeros, M., et al. 2003, AJ, 126, 2081

Agüeros, M.A., Ivezić, Ž., Covey, K.R., et al. 2005, AJ, 130, 1022

Anderson, S.F., Voges, W., Margon, B., et al. 2003, AJ, 126, 2209

Baldry, I.K, Glazebrook, K., Brinkmann, J., et al. 2004, ApJ, 600, 681

Baldwin, J., Phillips, M., & Terlevich, R. 1981, PASP, 93, 5

Becker, R.H., White, R.L., & Helfand, D.J. 1995, ApJ, 450, 559

Beichman, C.A., Neugebauer, G., Habing, H.J., Clegg, P.E. & Chester, T.J. 1985, *IRAS Catalogs and Atlases* (US GPO, Washington, DC)

Bell, E.F. 2003, ApJ, 586, 794

Bell, E.F., McIntosh, D.H., Katz, N. & Weinberg, M.D. 2003, ApJ, 585, L117

Best, P.N., Kauffmann, G., Heckman, T.M. & Ivezić, Ž. 2005a, MNRAS, 362, 9

Best, P.N., Kauffmann, G., Heckman, T.M., et al. 2005b, MNRAS, 362, 25

Blanton, M.R., Hogg, D.W., Bahcall, N.A., et al. 2003, ApJ, 592, 819

Brinchmann, J., Charlot, S., White, S.D.M., Tremonti, C., Kauffmann, G., Heckman, T., Brinkmann, J. 2004, MNRAS, 351, 1151

Bruzual, G. & Charlot, S. 1993, ApJ, 405, 538

Bruzual, G. & Charlot, S. 2003, MNRAS, 344, 1000

Buat, V., Iglesias-Páramo, J., Seibert, M., et al. 2005, ApJ, 619, 51

Cardelli, J.A., Clayton, G.C., & Mathis, J.S. 1989, ApJ, 345, 245

Chang, R., Gallazzi, A., Kauffmann, G., Charlot, S., Ivezić, Ž., Brinchmann, J. & Heckman, T.M. 2005, accepted by MNRAS (also astro-ph/0502117)

Condon, J.J., Cotton, W.D., Greisen, E.W., Yin, Q.F., Perley, R.A., Taylor, G.B., & Broderick, J.J. 1998, AJ, 115, 1693

Condon, J.J. & Broderick, J.J. 1988, AJ, 96, 30

Eisenstein, D.J., Hogg, D.W., Fukugita, M., et al. 2002, ApJ, 585, 694

Finlator, K., Ivezić, Ž., Fan, X., et al. 2000, AJ, 120, 2615

Fukugita, M., Ichikawa, T., Gunn, J.E., Doi, M., Shimasaku, K., & Schneider, D.P. 1996, AJ, 111, 1748

Goto, T. 2005, MNRAS, 360, 322

Gregory, P.C., Scott, W.K., Douglas, K., & Condon, J.J. 1996, ApJS, 103, 427

Gunn, J.E. & Oke, J.B. 1975, ApJ, 195, 255

Gunn, J.E., Carr, M., Rockosi, C., et al. 1998, AJ, 116, 3040

Hao, L., Strauss, M.A., Tremonti, C.A., et al. 2005, AJ, 129, 1783

Heckman, T.M., Kauffmann, G., Brinchmann, J., Charlot, S., Tremonti, C. & White, S.D.M. 2004, ApJ, 613, 109

Helou, G., Soifer, B.T.& Rowan-Robinson, M. 1985, ApJ, 298, 7

Hogg, D.W., Finkbeiner, D.P., Schlegel, D.J. & Gunn, J.E. 2002, AJ, 122, 2129

Hopkins, A.M., Miller, C.J., Nichol, R.C., et al. 2003, ApJ, 599, 971

Ivezić, Ž. & Elitzur, M. 1997, MNRAS 287, 799

Ivezić, Ž., Becker, R.H., Blanton, M. et al. 2001a, in AGN Surveys, IAU Colloq. 184, eds. R.F. Green, E.Ye.

Khachikian & D.B. Sanders (San Francisco: ASP), p. 137 (astro-ph/0111024)

Ivezić, Ž., Tabachnik, S., Rafikov, R., et al. 2001b, AJ, 122, 2749

Ivezić, Ž., Menou, K., Knapp, G.R., et al. 2002, AJ, 124, 2364

Ivezić, Ž., Siverd, R., Steinhardt, W., et al. 2004a, in Multiwavelength AGN Surveys, Guillermo Haro Conf., eds. Mújica, R. & Maiolino, R. (Conzumel, Mexico), p. 53 (astro-ph/0403314)

Ivezić, Ž., Lupton, R.H., Schlegel, D., et al. 2004b, AN, 325, No. 6-8, 583 (astro-ph/0410195)

Jarrett, T.H., Chester, T., Cutri, R., Schneider, S., Skrutskie, M., & Huchra, J.P. 2000, AJ, 119, 2498

Lupton, R.H., Ivezić, Ž., Gunn, J.E., Knapp, G.R., Strauss, M.A. & Yasuda, N. 2002, in "Survey and Other Telescope Technologies and Discoveries", eds. Tyson, J.A. & Wolff, S., Proceedings of the SPIE, 4836, 350

Kauffmann, G., Heckman, T.M., White, S.D.M., et al. 2003a, MNRAS, 341, 33

Kauffmann, G., Heckman, T.M., White, S.D.M., et al. 2003b, MNRAS, 341, 54

Kauffmann, G., Heckman, T.M., Tremonti, C.A., et al. 2003c, MNRAS, 346, 1055

Kewley, L., Jansen, R.A. & Geller, M.J. 2005, PASP 117, 227

McIntosh, D.H., Bell, E.F., Weinberg, M.D. & Katz, N. 2005, astro-ph/0511737

Moustakas, J., Kennicutt, R.C. & Tremonti, C.A. 2005, astro-ph/0511730

Nenkova, M., Ivezić, Ž., Elitzur, M. 2002, ApJ, 570, L9

Pasquali, A., Kauffmann, G. & Heckman, T.M. 2005, MNRAS, 361, 1121

Petrosian, V. 1976, AJ, 209, L1

Pier, J.R., Munn, J.A., Hindsley, R.B., Hennesy, G.S., Kent, S.M., Lupton, R.H. & Ivezić, Ž. 2003, AJ, 125, 1559

Rengelink, R.B., Tang, Y., de Bruyn, A.G., Miley, G.K., Bremer, M.N., Roettgering, H.J.A. & Bremer, M.A.R. 1997, A&AS, 124, 259

Richards, G.T., Fan, X., Newberg, H.J., et al. 2002, AJ, 123, 2945

Schlegel, D.J., Finkbeiner, D.P.; Davis, M. 1998, ApJ, 500, 525

Schmitt, H.R., Kinney, A.L., Calzetti, D. & Storchi Bergman, T. 1997, AJ, 114, 592

Shimasaku, K., Fukugita, M., Doi, M., et al. 2001, AJ, 122, 1238

Smith, J.A., Tucker, D.L., Kent, S.M., et al. 2002, AJ, 123, 2121

Smolčić, V., Ivezić, Ž., Gaćeša, M., et al. 2006, submitted to MNRAS

Stoughton, C., Lupton, R.H., Bernardi, M., et al. 2002, AJ, 123, 485

Strateva, I., Ivezić, Ž., Knapp, G.R., et al. 2001, AJ, 122, 1861

Strauss, M.A., Weinberg. D.H., Lupton, R.H., et al. 2002, AJ, 124, 1810

Tremonti, C.A., Heckman, T.M., Kauffmann, G., Brinchmann, J., Charlot, S., White, S.D.M., Seibert, M., Peng, E.W. Schlegel, D.J., Uomoto, A., Fukugita, M. & Brinkmann, J. 2004, ApJ, 613, 898

Voges, W.H., Aschenbach, B., Boller, Th., et al. 1999,

A&A, 349, 389

Voges, W.H., Aschenbach, B., Boller, Th., et al. 2000, IAU Circ., 7432, 1

van der Kruit, P. 1971, A&A, 15, 110

Yasuda, N., Fukugita, M., Narayanan, V.K., et al. 2001, AJ, 122, 1104

Yip, C.W., Connolly, A.J., Szalay, A. et al. 2004, AJ, 128, 585

York, D.G., Adelman, J., Anderson, S., et al. 2000, AJ, 120, 1579

Yun, M.S., Reddy, N.A. & Condon, J.J. 2001, ApJ, 554, 803

APPENDIX A: TECHNICAL SUMMARY OF THE ANALYZED SURVEYS

A1   Sloan Digital Sky Survey

SDSS (www.sdss.org) is a digital photometric and spectroscopic survey that will cover one quarter of the Celestial Sphere in the North Galactic cap and produce a smaller area (~ 225 deg^2), but much deeper, survey in the Southern Galactic hemisphere (York et al. 2000, Stoughton et al. 2002, Abazajian et al. 2003, and references therein). The flux densities of detected objects are measured almost simultaneously in five bands (u, g, r, i, and z, Fukugita et al. 1996, Hogg et al. 2002, Smith et al. 2002;) with effective wavelengths of 3551 Å, 4686 Å, 6166 Å, 7480 Å, and 8932 Å (Gunn et al. 1998), accurate to 0.02 mag (root-mean-square scatter for sources not limited by photon statistics, and also for zeropoints, Ivezić et al. 2004b). The survey will result in photometric measurements for close to 100 million stars and a similar number of galaxies. Astrometric positions are accurate to better than 0.1 arcsec per coordinate (rms) for sources with $r < 20.5^m$ (Pier et al. 2003), and the morphological information from the images allows reliable star-galaxy separation to $r \sim 21.5$ mag (Lupton et al. 2002). The imaging data are used to select sources for follow-up spectroscopic observations, which will result in over a million spectra. The spectra have a resolution of 1800-2000 in the wavelength range from 3800 to 9200 Å. Extragalactic sources targeted in the SDSS spectroscopic survey include a flux-limited "main" galaxy sample ($r<17.77$, Strauss *et al.* 2002), the luminous red galaxy sample (Eisenstein *et al.* 2002), and quasars (Richards *et al.* 2002).

A2   ROSAT Survey

The ROentgen SATellit (ROSAT, 1990-1999) was an X-ray observatory which included the X-Ray Telescope (XRT) with its 2.4 m focal-length mirror assembly consisting of four nested Wolter-I mirrors. The focal plane instrumentation consisted of the Position Sensitive Proportional Counter (PSPC) and the High Resolution Imager (HRI). The Wide-Field Camera (WFC) with its 0.525 m focal-length mirror assembly consisting of three nested Wolter-Schwarzschild mirrors (co-aligned with the XRT). XRT covered $\sim$6-100Å($\sim$2.4-0.12keV) band, and the WFC covered the $\sim$60-300Å ($\sim$0.21-0.05keV) band. ROSAT provided a $\sim$2 degree diameter field of view with the PSPC in the focal plane, and $\sim$40 arcmin diameter field of view with the HRI

in the focal plane. The main aim of the ROSAT mission was the first all-sky survey with imaging X-ray and XUV telescopes; its X-ray sensitivity was about a factor of 1000 higher than that of the UHURU satellite. About 100,000 sources have been detected in the survey, an order of magnitude more than were known before ROSAT (Voges et al. 1999, Voges et al. 2000).

A3   GALEX Survey

The Galaxy Evolution Explorer (GALEX) was launched in April 2003, and will eventually map the entire sky in two bands: the near ultraviolet (NUV; 1750–2800 Å) and the far ultraviolet (FUV; 1350–1750 Å), and to faint flux levels (m=20-25, AB). GALEX's 0.5 m telescope and 1.2° field of view will also be used to make deep observations (>tens of kiloseconds) of individual interesting fields (such as the Lockman Hole and the Chandra Deep Field–South). The mission's primary science goal is to observe star-forming galaxies and to track galaxy evolution. The GALEX Early Release Observations used here include three AIS fields (see www.galex.caltech.edu) which overlap with the SDSS footprint.

A4   2MASS Survey

2MASS used two 1.3-meter telescopes, one at Mt. Hopkins, AZ, and one at CTIO, Chile, to survey the entire sky in near-infrared light (see www.ipac.caltech.edu/2mass). Each telescope's camera was equipped with three 256×256 arrays (the pixel size is 2 arcsec) of HgCdTe detectors which simultaneously observed in the J (1.25 μm), H (1.65 μm), and K_s (2.17 μm) bands. The detectors were sensitive to point sources brighter than about 1 mJy at the 10σ level, corresponding to limiting (Vega-based) magnitudes of 15.8, 15.1, and 14.3, respectively. Point-source photometry is repeatable to better than 10% precision at this level, and the astrometric uncertainty for these sources is less than 0.2 arcsec. The 2MASS catalogs contain positional and photometric information for 470,992,970 point sources (2MASS PSC) and 1,647,599 extended sources (2MASS XSC). Details about 2MASS photometry of galaxies can be found in Jarrett et al. (2000).

A5   IRAS Survey

The Infrared Astronomical Satellite (IRAS, Beichman et al. 1985) produced an almost all-sky survey ($\sim$ 98% of the sky) at 12, 25, 60 and 100 μm, with the resulting IRAS point source catalog (IRAS PSC) containing over 250,000 sources, and the Faint Source Catalog additional 173,000 sources. While the IRAS faint limits are of order 1 Jy, it remains a valuable resource due to its important wavelength range and nearly full sky coverege.

A6   Radio Surveys

The basic properties of the radio surveys considered here are:

GB6: The Green Bank GB6 survey (GB6, Gregory et al. 1996) is at 4850 MHz (6 cm), with 3 arcmin resolution,

and covers the declination band between $0°$ and $75°$. The completeness limit of the GB6 catalog is 18 mJy, and it includes 75,000 sources.

NVSS: The NRAO VLA Sky Survey (NVSS, Condon et al. 1998) is a 1.4 GHz (20 cm) survey with 45 arcsec resolution, and covers the sky north of $-40°$ declination. The completeness limit of the NVSS catalog is about 2.5 mJy, and it includes 1.8 million sources.

FIRST: The Faint Images of the Radio Sky at Twenty-centimeters (FIRST, Becker, White & Helfand 1995) is a 1.4 GHz (20 cm) survey with 5 arcsec resolution, and will cover a quarter of the sky matched to the SDSS footprint. The completeness limit of the FIRST catalog is 1 mJy, and it will include about 1 million sources. The FIRST survey provides the highest resolution and most accurate radio positions among the large radio surveys. It also has the highest source density of about 90 $\deg^{-2}$.

WENSS: The Westerbork Northern Sky Survey (WENSS, Rengelink et al. 1997) is a 326 MHz (92 cm) survey with $54'' \times 54''\cos(\delta)$ resolution, and covers the sky north of $+30°$ declination. The completeness limit of the WENSS catalog is 18 mJy, and it includes 230,000 sources.